Late Cretaceous (100–89 Ma) magnesian charnockites with adakitic affinities in the Milin area, eastern Gangdese: Partial melting of subducted oceanic crust and implications for crustal growth in southern Tibet ☆

Lin Ma [a,b], Qiang Wang [a,*], Derek A. Wyman [c], Zheng-Xiang Li [d], Zi-Qi Jiang [a], Jin-Hui Yang [e], Guo-Ning Gou [a,b], Hai-Feng Guo [a,b]

[a] State Key Laboratory of Isotope Geochemistry, Guangzhou Institute of Geochemistry, Chinese Academy of Sciences, Guangzhou 510640, China
[b] University of Chinese Academy of Sciences, Beijing 100049, China
[c] School of Geosciences, The University of Sydney, NSW 2006, Australia
[d] ARC Centre of Excellence for Core to Crust Fluid Systems (CCFS) and the Institute for Geoscience Research (TIGeR), Department of Applied Geology, Curtin University, GPO Box U1987, Perth, WA 6845, Australia
[e] Institute of Geology and Geophysics, Chinese Academy of Science, Beijing 100029, China

ARTICLE INFO

ABSTRACT

Rapid Mesozoic–Early Cenozoic crustal growth in the Gangdese area, southern Tibet, has commonly been attributed to pre-collisional and syn-collisional underplating of mantle-derived magmas. Here, we report on adakitic magnesian charnockites (i.e., hypersthene-bearing diorites and granodiorites) near Milin, in eastern Gangdese, that provide new insights into the crustal growth process of the region. Zircon U–Pb analyses of seven charnockite samples indicate that they were generated in the Late Cretaceous (100–89 Ma). They exhibit variable SiO_2 (53.9 to 65.7 wt.%) contents, high Na_2O/K_2O (1.6 to 14.4) and Sr/Y (27.2 to 138.7) ratios, low Y (6.5 to 18.5 ppm), heavy rare earth element (e.g., Yb = 0.6 to 1.6 ppm) and Th (0.20–2.39 ppm) contents and Th/La (0.02–0.23) ratios, with relatively high $Mg^{\#}$ (46 to 56) and MgO (2.0 to 4.5 wt.%) values. They are characterized isotopically by high and slightly variable $\varepsilon_{Nd}(t)$ (+2.4 to +4.0) and $\varepsilon_{Hf}(t)$ (+10.1 to +15.8) values with relatively low and consistent $(^{87}Sr/^{86}Sr)_i$ (0.7042 to 0.7043) ratios. Their pyroxenes have high crystallization temperatures (876 to 949 °C). The Milin charnockites were most probably produced by partial melting of subducted Neo-Tethyan oceanic crust that was followed by adakitic melt–mantle interaction, minor crustal assimilation and fractional crystallization of amphibole + plagioclase. The upwelling asthenosphere, triggered by the roll-back of subducted Neo-Tethyan oceanic lithosphere, provided the heat for slab melting. Therefore, we suggest that, in addition to pre-collisional and syn-collisional underplating of mantle-derived magmas, the recycling of subducted oceanic crust has also played an important role in continental crustal growth in southern Tibet.

1. Introduction

The Earth differs from other planets in our solar system in that it possesses continental crust (e.g., Hawkesworth and Kemp, 2006). The relative contributions of individual continental crust-forming processes, however, remain the topic of considerable debate (e.g., Hawkesworth and Kemp, 2006; Rudnick, 1995). Various processes have been proposed for the growth of continental crust, such as partial melting of underplated basaltic lower crust, subduction erosion, lower crustal delamination and recycling of oceanic lithosphere (e.g., Atherton and Petford, 1993; Clift

and Vannucchi, 2004; Clift et al., 2009; Jahn et al., 2000; Rudnick, 1995; Tang et al., 2012). Despite arguments that the volume of the continental crust has been essentially uniform since the Precambrian (particularly since 2.5 Ga) (e.g., Armstrong, 1991; Fyfe, 1978; Jahn et al., 2000), Phanerozoic juvenile crust has been increasingly recognized in recent decades (e.g., Jahn et al., 2000; Wang et al., 2007; Wu et al., 2000).

The well-known Gangdese batholith in the southern Lhasa block mainly consists of Jurassic–Early Eocene intermediate-felsic intrusive rocks (especially granites) (Fig. 1; Chu et al., 2006; Chung et al., 2005; Debon et al., 1986; Harris et al., 1990; Ji et al., 2009a,b; Wen et al., 2008a,b; Zhu et al., 2011, 2012, and references therein). Numerous studies have shown that the Gangdese batholith is characterized by high and positive $\varepsilon_{Nd}(t)$ (up to +5.5) and $\varepsilon_{Hf}(t)$ (up to +16.5) values (Chu et al., 2006, 2011; Chung et al., 2005; Harris et al., 1988a,b; Ji et al., 2009a,b; Ma et al., 2013-a,b; Mo et al., 2007; Wen et al., 2008a, b; Zhu et al., 2011), indicating remarkable crustal growth in the Phanerozoic. Previous studies have indicated that large-scale Cenozoic and
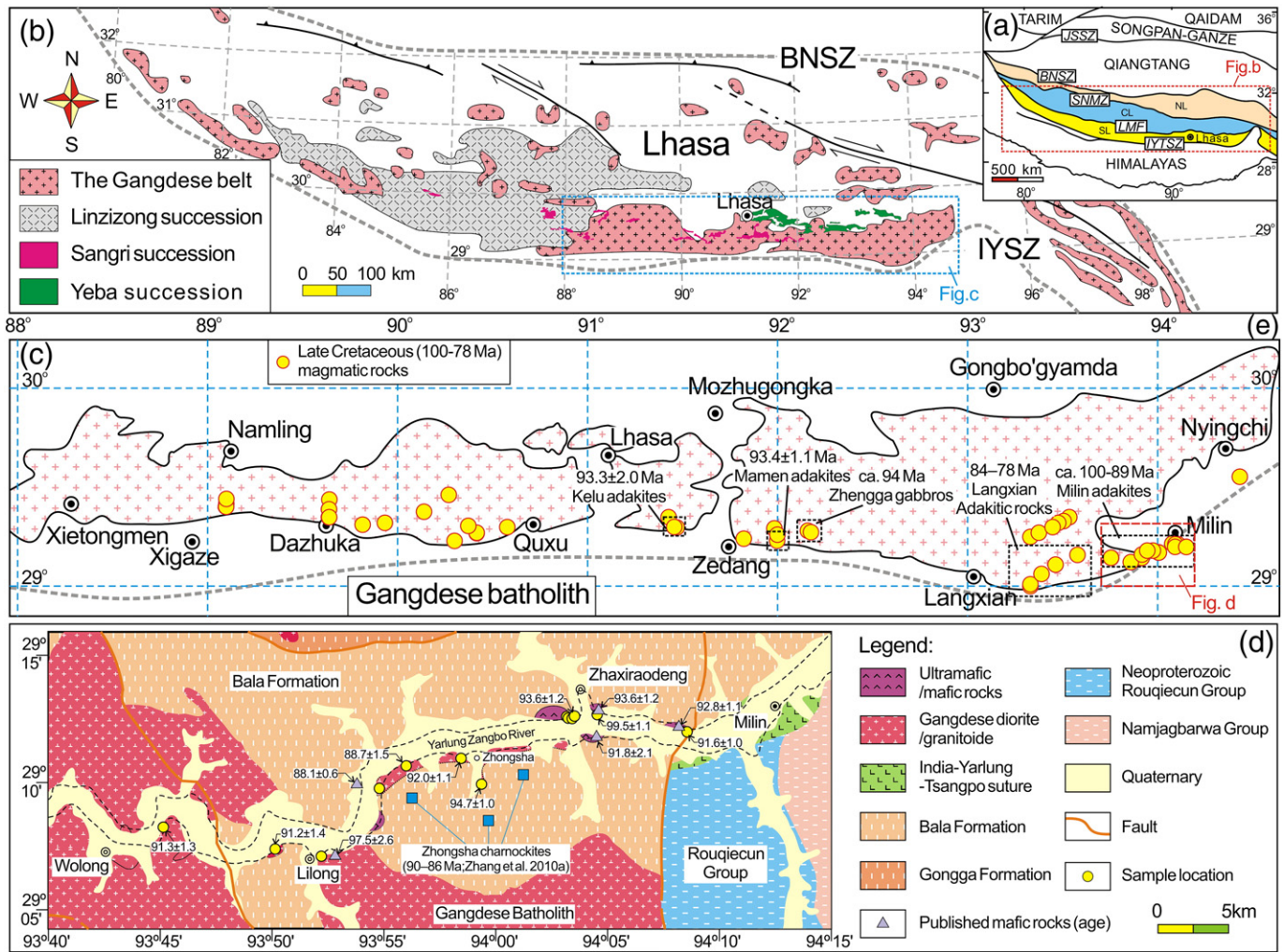
Fig. 1. (a) Diagram showing the Lhasa block in the context of the Tibetan Plateau (modified from Zhu et al. (2011)). (b) Geological map of the Lhasa block (modified from Chung et al. (2009)). (c) Detailed occurrences of Late Cretaceous (ca. 100–78 Ma) magmatic rocks from the Xietongmen–Nyingchi section of the Gangdese batholith with sampling locations (modified from Ma et al. (2013)). (d) Geological map of the Milin area, southern Tibet (modified from Yin et al. (in press)), showing the sampling locations and ages. The data of Late Cretaceous (~100–78 Ma) mgmatic rocks in Fig. 1(c) were collected from these references (Chu et al., 2006; Geng et al., 2006; Guan et al., 2010, 2011; Guo, 2011; Guo et al., 2011; Ji et al., 2009a,b; Jiang et al., 2012; Kang et al., 2010; Ma et al., 2013-a,b; Qu et al., 2007; Quidelleur et al., 1997; Scharer et al., 1984; Wen et al., 2008a,b; Xu, 2010; Zhang et al., 2010a; Zhu et al., 2011, this study and our unpublished data). The data of 84–78 Ma Langxian adakitic rocks are from Wen et al. (2008b) and Guan et al. (2010). The data of 90–86 Ma Zhongsha charnockites are from Zhang et al. (2010a). Abbreviations here are: JSSZ = Jinsha suture zone; BNSZ = Bangong–Nujiang suture zone; SNMZ = Shiquan River–Nam Tso Mélange Zone; LMF = Luobadui–Milashan Fault; IYSZ = Indus–Yarlung Suture Zone; SL = Southern Lhasa sub-block, CL = Central Lhasa sub-block; and NL = Northern Lhasa sub-block.

early Late Cretaceous (ca. 100–80 Ma) underplating from mantle-derived magmas played an important role in crustal growth of southern Tibet (e.g., Guan et al., 2010, 2011; Ji et al., 2009a,b; Ma et al., 2013-a,b; Mo et al., 2005, 2006, 2007; Wen et al., 2008a,b; Zhang et al., 2010a; Zhu et al., 2011). However, the triggering mechanism for these mainly Late Cretaceous magmatic events, and the crustal growth associated with them, remains a highly controversial issue with little consensus. For example, geodynamic models proposed to account for early Late Cretaceous magmatism and the tectonic evolution of the southern Lhasa block include low-angle or flat oceanic slab subduction (e.g., Coulon et al., 1986; Wen et al., 2008a,b), oceanic ridge subduction (e.g., Guan et al., 2010, 2011; Zhang et al., 2010a, 2011; Zhu et al., 2011, 2012) and roll-back of subducted oceanic slab (e.g., DeCelles et al., 2007; Ma et al., 2013-a).

Charnockites are broadly defined as granitoids containing orthopyroxene (or fayalite + quartz) and, typically, perthite, meso-perthite or antiperthite (Le Maitre, 2002). The distinctive conditions associated with their formation (low aH_2O (±high CO_2), high temperature) and their atypical granitoid mineral assemblages (Opx or fayalite and commonly Cpx) provide unique criteria for deciphering the tectonic events associated with their petrogenesis (e.g., Feio

et al., 2013; Frost et al., 2000; Grantham et al., 2012; Janardhan et al., 1982). Zhang et al. (2010a,b) first reported Late Cretaceous (90–85 Ma) charnockites associated with the Gangdese batholith, in the Zhongsha area (Fig. 1). In this paper, we report on adakitic charnockites (hypersthene-bearing diorites and granodiorites) from the Milin area, eastern Gangdese batholith (Fig. 1). We present detailed petrology, mineral compositions, geochronology that extends the known age range of the charnockites (100–89 Ma), whole rock major and trace element data that expands on the previously reported compositional range for charnockites in the region, and the first Sr–Nd–Hf isotope data for these rocks. The results offer an important opportunity to delineate the tectonic evolution and genetic relationships between early Late Cretaceous geodynamic processes and crustal growth in the Gangdese area, southern Tibet.

2. Geological background and rock characteristics

From south to north, Tibet consists of the Himalaya, Lhasa, Qiangtang, Songpan–Ganze, and Kunlun–Qaidam blocks (Fig. 1a). The Lhasa block is bounded by the Indus–Yarlung Tsangpo suture (IYS) to the south and the Bangong–Nujiang suture (BNS) to the north (Fig. 1a) (Yin and

Harrison, 2000). It is generally accepted that the BNS formed during the Late Jurassic–Middle Cretaceous (Yin and Harrison, 2000). The IYS has been ascribed ages ranging from the Late Cretaceous to latest Eocene (>65 Ma to <40 Ma) and remains the subject of debate (Aitchison et al., 2000, 2007, 2008; Dewey et al., 1988; Garzanti, 2008; Zahirovic et al., 2012). The IYS marks the closure of the Tethys, and lies on the southern boundary of an extensive Andean-type calc-alkaline magmatic belt (the Yeba, Sangri, Linzizong volcanic rocks and Gangdese batholith) in the Lhasa block (Fig. 1b) (e.g., Coulon et al., 1986; Mo et al., 2008; Murphy et al., 1997; Scharer et al., 1984; Zhu et al., 2008). Based on the distribution of different sedimentary cover rocks and ophiolites, the Lhasa block has recently been divided into northern, central, and southern sub-blocks, separated by the Shiquan River-Nam Tso Mélange Zone (SNMZ) and the Luobadui–Milashan Fault (LMF), respectively (Fig. 1a) (Pan et al., 2006; Zhu et al., 2011).

The Trans-Himalayan magmatic belt exposed along the southern margin of the Lhasa block extends from the Kohistan–Ladakh batholith in the west through the Gangdese batholith to the Chayu–western Yunnan–Burma batholith in the east, with a total length of over 3000 km (e.g., Yin and Harrison, 2000). The Gangdese batholith, mainly consisting of Jurassic–Early Eocene intermediate-felsic intrusive rocks, is the largest individual body in the Trans-Himalayan magmatic belt and one of the most important constituents of the southern Lhasa sub-block (e.g., Chu et al., 2006; Chung et al., 2003, 2009; Debon et al., 1986; Harris et al., 1990; Ji et al., 2009a; Wen et al., 2008a,b). Recent studies on Gangdese intermediate-felsic intrusive rocks demonstrated that an early Late Cretaceous (ca. 100–80 Ma) magmatic "flare-up" took place in the southern Gangdese area (Chu et al., 2006; Chung et al., 2005; Harris et al., 1988a,b; Ji et al., 2009a; Ma et al., 2013-a; Mo et al., 2007; Wen et al., 2008a,b; Zhu et al., 2011, 2012). Some Late Cretaceous mafic intrusive rocks in the Gangdese were also reported, e.g., ~94 Ma Gabbros and diorites in the Zhengga area, central Gangdese (Ma et al., in press-b), and 98–88 Ma mafic intrusive rocks and ~94–92 Ma Milin norites and hornblendites in the Milin and Langxian area, eastern Gangdese (Guan et al., 2011; Ma et al., 2013-a). Such Late Cretaceous mafic–felsic magmatic rocks are widely distributed along the southern margin of the Gangdese region (south of 29° 30′ N) in proximity to the IYS (e.g., Ma et al., 2013-a; Zhu et al., 2012) (Fig. 1c).

In this study, we report on newly identified charnockites (hypersthene-bearing diorites and granodiorites) in the Milin area, outcropping on both the south and north sides of the Yarlung Zangbo River and intruding the Bala Formation of the Nyainqentanglha Group (Fig. 1d). They are composed of diorites and granodiorites with a heterogeneous granular texture (Fig. 2a, b). These intrusive rocks are closely associated with the norite–hornblendite suites (Ma et al., 2013-a) (Fig. 2a, b). The diorites and granodiorites exhibit a gradual transitional relationship, indicating that they formed coevally. The diorites display massive structure with granular or mosaic texture (Fig. 2a, c) and generally consist of plagioclase (35–45 vol.%), hypersthene (10 vol.%), clinopyroxene (5–10 vol.%), amphibole (20–30 vol.%), quartz (5 vol.%) and minor biotite and magnetite (3–5 vol.%) (Fig. 2a, c, d). The subhedral–anhedral hypersthene and clinopyroxene grains are closely associated with plagioclase and amphibole (Fig. 2c, d), suggesting that they are early crystallization magmatic minerals. The granodiorites show subhedral granular texture and comprise plagioclase (50 vol.%), quartz (15 vol.%), hypersthene (10–15 vol.%), clinopyroxene (10 vol.%), high-Ti biotite (5 vol.%) with minor epidote, magnetite and titaniferous magnetite (Fig. 2e, f). The lack of reaction rims between the pyroxenes and associated minerals (plagioclase and biotite) indicates that the latter are primary igneous minerals (Fig. 2e, f).

3. Analytical methods

All silicate mineral analyses were carried out at the State Key Laboratory of Isotope Geochemistry, Guangzhou Institute of Geochemistry, Chinese Academy of Sciences (SKLIG GIG CAS) using a JXA-8100 electron microprobe. An accelerating voltage of 15 kV, a specimen current of 2.0×10^{-8} A, and a beam size of 1–2 μm were employed. The analytical errors are generally less than 2%. The analytical procedures were described in detail in Huang et al. (2007).

Zircons were separated using standard density and magnetic separation techniques. Zircon grains were handpicked and mounted in an epoxy resin disk, and then polished and coated with gold. Cathodoluminescence (CL) images were taken at SKLIG GIG CAS with a JEOL JXA-8100 Superprobe for inspecting internal morphology of individual zircons and for selecting positions for U–Pb and Lu–Hf isotope analyses. Zircon U–Pb dating was conducted at the MC-ICPMS laboratory of the Institute of Geology and Geophysics, Chinese Academy of Sciences (IGG CAS) in Beijing. Detailed operating conditions for the laser ablation system and the ICP-MS instrument and data reduction were the same as those described in Xie et al. (2008). An Agilent 7500a quadruple (Q)-ICPMS and a Neptune multi-collector (MC)-ICPMS with a 193 nm excimer ArF laser-ablation system (GeoLas Plus) attached were used for simultaneous determination of zircon U–Pb ages.

In situ Hf isotope measurements were subsequently undertaken using LA-ICPMS with a beam size of 60 μm and laser pulse frequency of 8 Hz with age determinations at the MC-ICPMS laboratory of IGG CAS. Details of instrumental conditions and data acquisition were given in Wu et al. (2006). The isobaric interference of ^{176}Lu on ^{176}Hf is negligible due to the extremely low $^{176}Lu/^{177}Hf$ in zircon (normally < 0.002). During the analyses for this study, GJ-1 as an unknown sample yielded a weighted $^{206}Pb/^{238}U$ age of 609.7 ± 6.3 Ma (2σn, MSWD = 0.97, n = 12) and a weighted $^{176}Hf/^{177}Hf$ ratio of 0.282015 ± 0.000003 (2σn, MSWD = 1.12, n = 94), which is in good agreement with the recommended U–Pb age and Hf isotopic ratio (Black et al., 2003; Wu et al., 2006). During data acquisition of Hf isotopes, $^{176}Hf/^{177}Hf$ ratios of the zircon standard (MUD) were 0.282504 ± 0.000003 (2σn, MSWD = 0.71, n = 82).

Rock samples were examined by optical microscopy and selected whole-rock samples were sawed into small chips and ultrasonically cleaned in distilled water with <3% HNO_3 and then in distilled water alone, and subsequently dried and handpicked to remove visible contamination. The rocks were crushed and ground in a tungsten carbide ring mill, and the resulting powder was used for analyses of major and trace elements, and Sr–Nd isotopes, at SKLIG GIG CAS. Major-element oxides were analyzed using a Rigaku RIX 2000 X-ray fluorescence spectrometer at SKLIG, GIG-CAS on fused glass beads. Calibration lines used in quantification were produced by bivariate regression of data from 36 reference materials encompassing a wide range of silicate compositions (Li et al., 2005), and analytical uncertainties are between 1% and 5%. Trace elements were analyzed by inductively coupled plasma mass spectrometry (ICP-MS), using a Perkin-Elmer Sciex ELAN 6000 instrument at SKLIG GIG CAS. Analytical procedures are the same as those described by Li et al. (2002). Repeated runs give <3% RSD (relative standard deviation) for most elements of reference materials for ICP-MS analysis.

Sr and Nd isotopic compositions of selected samples were determined using a Micromass Isoprobe multi-collector mass spectrometer (MC-ICP-MS) at SKLIG, GIG-CAS. Analytical procedures are similar to those described in Li et al. (2004) and Wei et al. (2002). The $^{87}Sr/^{86}Sr$ ratio of the NBS987 standard and $^{143}Nd/^{144}Nd$ ratio of the Shin Etsu JNdi-1 standard measured were 0.710288 ± 28 (2σ m) and 0.512115 ± 7 (2σ m; Tanaka et al., 2000), respectively. All measured $^{143}Nd/^{144}Nd$ and $^{86}Sr/^{88}Sr$ ratios are fractionation corrected to $^{146}Nd/^{144}Nd$ =0.7219 and $^{86}Sr/^{88}Sr$ = 0.1194, respectively.

4. Results

4.1. Zircon U–Pb geochronology

The LA-ICP-MS in situ zircon U–Pb isotopic data are given in Supplementary file 1. Zircons from the two granodiorite and five
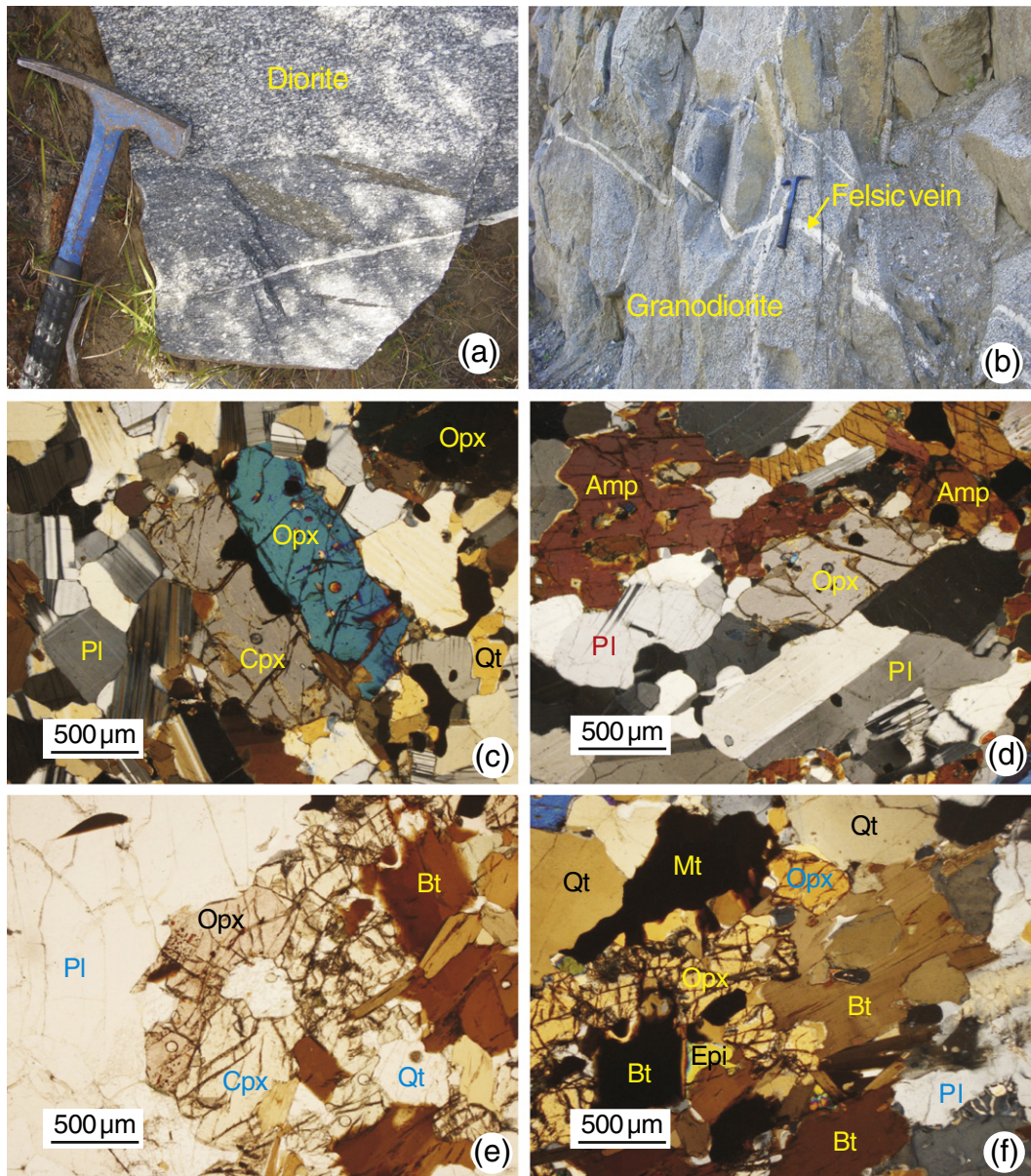
Fig. 2. Field geological observation and petrography (plane-polarized light) of the Milin intrusive rocks: (a) the massive diorites; (b) the massive granodiorites with some felsic veins; (c) orthopyroxenes and clinopyroxenes in the Milin diorites; (d) main mineral assemblage of the diorites; (e) orthopyroxenes and clinopyroxenes in the Milin granodiorites; (f) main mineral assemblage of the granodiorites. Abbreviations: Pl, plagioclase; Amp, amphibole; Bt, biotite; Cpx, clinopyroxene; Opx, orthopyroxene; Epi, epidote; Qt, quartz.

diorite samples have crystal lengths of ~100–300 μm and length-to-width ratios from 1:1 to 2:1, respectively (Fig. 3). The analyzed zircon grains from seven samples have variable U (17.7–541 ppm) and Th (9.2–606 ppm) contents, with Th/U ratios ranging from 0.29 to 1.34, indicating a magmatic origin (Hoskin and Black, 2000).

Zircon U–Pb age data for the seven samples are shown in Fig. 3. Thirteen and sixteen zircon U–Pb analyses for granodiorite samples 09 TB36 and 09 TB45-1 yielded concordant $^{206}Pb/^{238}U$ ages of 97 to 100 Ma and 92 to 97 Ma, with weighted mean ages of 99.5 ± 1.1 Ma (MSWD = 0.11) and 94.7 ± 1.0 Ma, respectively (Fig. 3f, g; Supplementary file 1). Sixteen zircon U–Pb analyses for diorite sample 09 TB47-1 gave concordant $^{206}Pb/^{238}U$ ages of 83 to 91 Ma, with a weighted mean age of 88.5 ± 1.5 Ma (Fig. 3c). Fifteen, fourteen, thirteen and fourteen analyses were conducted on the other four diorite samples (09 TB21-2, 09 TB42-1, 09 TB46-2 and 09 TB51-2), respectively, giving weighted mean ages of 91.6 ± 1.0 Ma, 93.6 ± 1.2 Ma, 92.0 ± 1.1 Ma and 91.2 ± 1.4 Ma. Thus, LA-ICP-MS in situ zircon U–Pb dating for the

seven samples suggests that these rocks were generated in the early Late Cretaceous (100–89 Ma) (Fig. 3, Supplementary file 1) and were approximately contemporaneous with, though slightly earlier than, the 90–86 Ma Zhongsha charnockites (Zhang et al., 2010a). Collectively, the U–Pb data indicate that charnockites in the eastern Gangdese area were emplaced over a somewhat longer period (100 to 86 Ma) than previously recognized.

4.2. Mineral compositions

Major oxide compositions of clinopyroxene and orthopyroxene are listed in Table 1. Clinopyroxenes grains in the diorites and granodiorites mainly consist of augite and diopside, with compositions of $Wo_{41.0–45.6}En_{35.0–37.6}Fs_{15.7–19.2}$ and $Wo_{41.0–45.6}En_{34.6–38.2}Fs_{14.0–18.6}$, respectively (Table 1). Clinopyroxene grains from the granodiorites display slightly more variable chemical compositions (Mg-number [$Mg^\# = Mg^{2+} / (Fe^{2+} + Mg^{2+}) \times 100$] = 70.9–76.4; SiO_2 = 48.83–
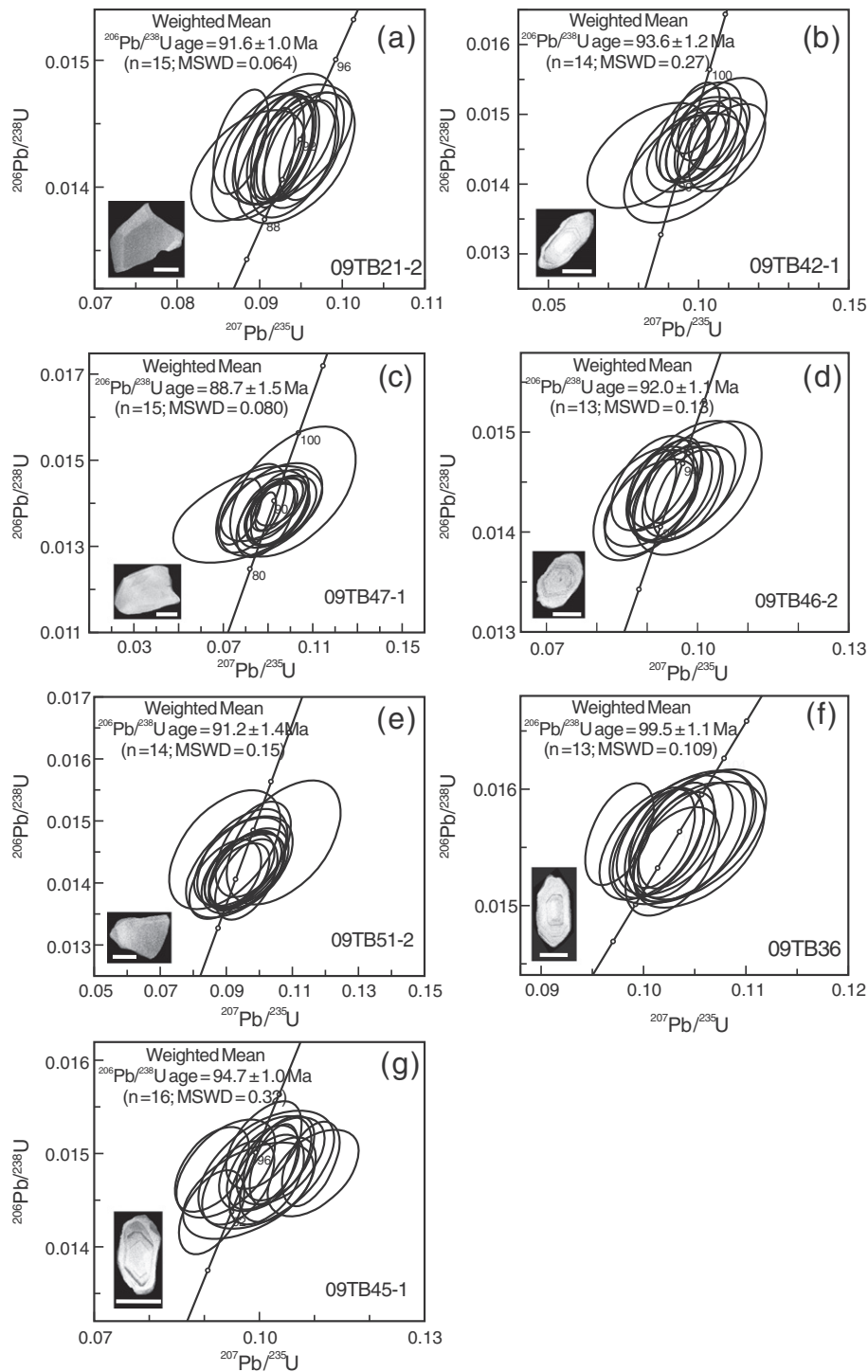
Fig. 3. Zircon U–Pb Concordia diagram of the Milin charnockites in eastern Gangdese, southern Tibet. The representative cathodoluminescence (CL) images in inset and the white segments represent 100 μm.

52.77 wt.%) than those from the diorites ($Mg^{\#}$ = 70.3–73.7; SiO_2 = 50.31–51.34 wt.%). All orthopyroxene grains are hyperstheness, with a composition of $Wo_{1.0–2.3}En_{55.6–61.5}Fs_{36.9–42.3}$ (Table 1). The hypersthene grains in the granodiorites also have slightly variable chemical compositions and relatively high $Mg^{\#}$ ($Mg^{\#}$ = 62.7–66.2; SiO_2 = 47.52–53.58 wt.%) compared to those of the diorites ($Mg^{\#}$ = 61.0–64.1; SiO_2 = 50.40–52.23 wt.%). Plagioclase from the diorites mainly consists of andesine ($Ab_{49.8–60.46}An_{36.3–48.3}$) and minor oligoclase ($Ab_{77.0}An_{22.7}$). Plagioclase from the granodiorites is composed of andesine with compositions of $Ab_{64.2–65.7}An_{31.3–32.6}$.

4.3. Major and trace element geochemistry

Chemical compositions of the Milin diorites and granodiorites are listed in Table 2. They have variable SiO_2 (53.9–65.7 wt.%), high Al_2O_3 (16.4–21.1 wt.%), and TiO_2 (0.7–0.9 wt.%) contents. They are characterized by variable $Mg^{\#}$ (36–56) values, Cr (3.5–95.5 ppm) and Ni (6.5–44.1 ppm) contents (Table 2). On a total alkalis versus silica (TAS) diagram, the Milin intrusive rock samples plot in the fields of gabbroic diorites, diorites and granodiorites (Fig. 4a). Gabbroic diorites and diorites are hereinafter referred as diorites. Apart from one sample

Table 1

Representative electron probe analyses of clinopyroxene and orthopyroxene phenocrysts.

Sample	SiO$_2$	TiO$_2$	Al$_2$O$_3$	FeO*	MnO	MgO	CaO	Na$_2$O	K$_2$O	Cr$_2$O$_3$	Total	Mg#	Wo	En	Fs
Othropyroxene															
09TB51-2 (2)	50.75	0.03	1.19	25.98	1.06	20.36	0.54	0.08	0.02	0.04	100.05	62.17	1.07	56.74	41.89
09TB51-2 (3)	50.40	0.02	1.35	25.61	1.03	20.19	1.14	0.06	–	0.02	99.80	62.31	2.29	56.27	41.24
09TB51-2 (11)	50.99	0.05	1.35	25.98	1.22	20.15	0.60	0.04	0.01	0.01	100.40	61.93	1.21	56.33	42.34
09TB51-2 (17)	51.02	0.03	1.31	24.83	1.03	20.38	0.56	0.12	0.03	0.03	99.36	63.25	1.14	57.62	40.78
09TB51-2 (21)	51.32	0.09	1.32	24.52	1.10	20.90	0.65	0.03	0.02	0.01	99.96	64.13	1.32	58.55	40.02
09TB51-2 (22)	51.17	0.06	1.32	24.45	1.05	20.62	0.66	0.05	0.01	0.02	99.41	63.87	1.33	58.26	40.22
09TB51-2 (26)	50.58	0.04	1.33	26.23	0.97	20.30	0.57	0.06	0.02	0.02	100.11	61.88	1.13	56.56	42.09
09TB45-2 (1)	50.89	0.08	1.19	24.95	1.18	20.00	0.60	0.15	0.06	0.17	99.26	62.70	1.22	56.82	41.41
09TB45-2 (12)	51.80	0.06	1.28	23.27	1.36	20.83	0.61	0.05	0.02	0.01	99.27	65.25	1.24	59.30	39.29
09TB45-2 (14)	52.41	0.06	1.30	24.36	1.35	19.97	0.65	0.06	0.05	0.07	100.27	63.23	1.33	57.16	41.31
09TB45-2 (21)	53.58	0.12	1.26	23.51	1.09	20.39	0.51	0.09	0.03	0.03	100.61	64.53	1.06	58.67	39.92
09TB45-2 (22)	53.23	0.05	1.19	22.60	1.06	21.33	0.71	0.07	0.02	0.05	100.32	66.43	1.44	60.54	37.75
09TB45-2 (29)	51.60	0.10	1.11	24.16	1.02	21.22	0.65	0.06	0.02	0.02	99.95	64.81	1.30	59.25	39.21
09TB45-2 (30)	51.31	0.06	1.20	23.17	1.10	21.67	0.57	0.07	0.01	0.07	99.22	66.24	1.14	60.71	37.89
Clinopyroxene															
09TB50 (4)	51.24	0.10	1.95	10.76	0.61	12.69	21.95	0.71	0.03	0.01	100.05	71.21	44.18	35.53	17.69
09TB50 (1)	50.85	0.16	1.30	10.03	0.64	13.32	22.58	0.63	0.02	–	99.52	73.58	44.74	36.71	16.29
09TB50 (3)	51.03	0.01	1.62	10.30	0.78	12.69	23.01	0.73	–	–	100.17	72.10	45.54	34.95	16.89
09TB51-2 (4)	50.31	0.10	1.91	9.84	0.44	13.16	22.94	0.60	0.04	0.00	99.34	73.73	45.64	36.44	15.74
09TB51-2 (10)	50.89	0.11	1.42	11.30	0.53	13.31	21.50	0.56	0.01	0.03	99.65	71.17	42.87	36.92	18.20
09TB51-2 (14)	51.34	0.13	1.24	10.15	0.46	13.56	23.45	0.49	–	0.01	100.83	73.69	45.64	36.72	15.91
09TB51-2 (15)	50.99	0.13	1.67	12.14	0.51	13.67	20.77	0.62	0.01	0.01	100.53	70.26	41.01	37.55	19.23
09TB45-2 (5)	50.96	0.07	2.01	10.25	0.58	13.03	22.76	0.92	–	0.01	100.59	72.72	44.73	35.63	16.36
09TB45-2 (7)	50.50	0.07	2.22	10.66	0.58	13.45	22.03	0.90	0.05	0.04	100.49	72.56	43.21	36.68	16.91
09TB45-2 (8)	51.37	0.07	1.66	10.13	0.59	13.40	22.53	0.79	0.01	0.04	100.57	73.51	44.30	36.67	16.23
09TB45-2 (9)	50.88	0.09	1.64	10.14	0.54	13.55	22.27	0.78	0.01	0.01	99.90	73.70	43.89	37.15	16.18
09TB45-2 (19)	50.67	0.13	2.28	8.57	0.48	13.20	22.97	0.90	0.02	0.00	99.23	76.35	45.99	36.77	13.96
09TB45-2 (24)	51.31	0.15	1.51	9.40	0.43	13.12	22.78	0.73	0.03	–	99.46	74.53	45.62	36.55	15.20
09TB45-2 (28)	51.87	0.11	1.81	9.26	0.42	13.07	22.82	0.83	0.01	0.02	100.20	74.76	45.64	36.38	14.97

(09TB47-1) with the lowest K$_2$O content (0.36 wt.%), other diorite and granodiorite samples have medium K$_2$O (0.78–2.08 wt.%) and low K$_2$O/Na$_2$O (0.20–0.49) values (Figs. 4b and 8a; Table 2), and plot within the medium-K calc-alkaline field on the SiO$_2$ versus K$_2$O diagram (Fig. 4b) and in the low-Fe and medium-Fe fields on the SiO$_2$ versus FeO$_{total}$/MgO diagram (Fig. 4a).

The Milin diorites and granodiorites display low concentrations of heavy rare earth elements (HREEs) and Y (e.g., Yb = 0.58–1.7 ppm; Y = 6.5–18.5 ppm) and high Sr (456–907 ppm) contents with high Sr/Y (27.2–139) and La/Yb (6.0–12.3) ratios, indicating that they have adakitic affinities (Fig. 4d; Table 2) as defined by Defant and Drummond (1990). The granodiorite samples have higher Sr, Sr/Y and La/Yb values than those of most diorite samples with the exception of one sample 09TB47-1 (Figs. 4d, 5; Table 2). On the chondrite-normalized rare earth element (REE) diagrams, the diorite samples show subparallel patterns with relatively enriched ([La/Yb]$_N$ = 4.3–7.1) light REEs (LREEs) and slightly depleted HREEs ([Gd/Yb]$_N$ = 1.5–2.0) (Fig. 5a). Apart from two samples (09TB47-1 and 09TB51-2) with obvious positive Eu anomalies (Eu/Eu* ($Eu_N/\sqrt[2]{Sm_N \times Gd_N}$) = 1.51 and 1.28), other diorite samples display negligible Eu anomalies (Eu/Eu* = 0.87–1.16) (Fig. 5a). These diorites are geochemically characterized by the enrichment of large ion lithophile elements (LILEs) and the depletion of HFSEs (Fig. 5b). The granodiorites display more variable REEs ([La/Yb]$_N$ = 7.3–10.4) with no to clearly positive Eu anomalies (Eu/Eu* = 1.00–1.21) (Fig. 5c). All diorites and granodiorites exhibit strong negative Ta–Nb–Ti anomalies (e.g., [Nb/La]$_N$ = 0.18–0.38) and positive Sr anomalies (Fig. 5d).

4.4. Sr–Nd–Hf isotope geochemistry

Initial isotopic ratios of the Milin diorites and granodiorites were calculated based on the mean formation age of 92.8 Ma, and the whole rock Sr–Nd and zircon Hf isotopic composition data are given in Table 3 and Supplementary file 2, respectively. The Milin diorites and granodiorites exhibit low and constant initial ^{87}Sr/^{86}Sr isotopic

ratios (0.7042–0.7043) and slightly variable $\varepsilon_{Nd}(t)$ values (+2.4 to +4.0, average +3.4), which are comparable to those of the Tethyan basalts (e.g., Mahoney et al., 1998; Xu and Castillo, 2004; Zhang et al., 2005) (Fig. 6a). They display $\varepsilon_{Nd}(t)$ values that are relatively high, compared to those of Late Cretaceous (94 Ma) gabbros in the Zhengga area (Figs. 1c, 6a) (Ma et al., in press-b) and Late Cretaceous (84–78 Ma) adakitic rocks generated by melting of thickened juvenile mafic lower crust in the Langxian area (Figs. 1c, 6a) (Wen et al., 2008b). They have high and variable $\varepsilon_{Hf}(t)_{zircon}$ values (+10.1 to +15.8) and positive $\Delta\varepsilon_{Hf}(t)$ values (+4.5 to +8.2) [where $\Delta\varepsilon_{Hf}(t) = \varepsilon_{Hf}(t) - (1.59\varepsilon_{Nd}(t) + 1.28)$] and plot close to or above the mantle array [$\varepsilon_{Hf}(t) = 1.59\varepsilon_{Nd}(t) + 1.28$] of Chauvel et al. (2008) in the $\varepsilon_{Hf}(t)$ versus $\varepsilon_{Nd}(t)$ diagram (Fig. 6c). They also have high and positive $\varepsilon_{Hf}(t)_{zircon}$ values, overlapping with those of zircons from the Ladakh − Kohistan batholiths (Fig. 6c; Ravikant et al., 2009; Schaltegger et al., 2002).

5. Discussion

5.1. Rock types and tectonic setting

The Milin adakitic charnockites display low FeO / (FeO + MgO) (0.58–0.67) (Fig. 7a) and A/CNK (0.80–1.01, except for samples 09TB45-2 and 09TB41-1 with values of 1.07 and 1.10, respectively) (Table 2 and Fig. 7a). The Milin adakitic charnockites and the Zhongsha charnockites (Zhang et al., 2009, 2010b) are magnesian and calcic to calc-alkalic (Fig. 7a–b), consistent with their generation in an arc setting (Frost and Frost, 2008). Other evidence also support a setting related to the subduction of the Neo-Tethyan oceanic lithosphere, such as: (1) the occurrence of the Late Cretaceous Indus–Yarlung Tsangpo ophiolites (e.g., Malpas et al., 2003; Zhang et al., 2005); (2) the recognition of Late Cretaceous (ca. 90 Ma) Gangdese belt adakites generated by melting of subducted slab (e.g., Jiang et al., 2012; Kang et al., 2010; Zhang et al., 2010b); and (3) the arc magmatic affinity of all early Late Cretaceous magmatic rocks of the Gangdese batholith, including mafic rocks (e.g., the enrichment of LREE, LILE and negative Nb–Ta–

Table 2
Major (wt %) and trace element (ppm) data for the Milin granitoids.

Sample	09TB21-2	09TB22	09TB38-1	09TB39	09TB40	09TB41-3	09TB42-1	09TB45-3	09TB46-1	09TB46-2	09TB47-1
Rock type	Diorite	Diorite	Diorite	Diorite	Diorite	Diorite	Diorite	Diorite	Diorite	Diorite	Diorite
Longitude	94° 08′ 37″	94° 08′ 32″	94° 03′ 33″	94° 03′ 26″	94° 03′ 19″	94° 03′ 15″	94° 03′ 10″	93° 59′ 22″	93° 58′ 27″	93° 58′ 27″	93° 56′ 00″
Latitude	29° 12′ 00″	29° 12′ 01″	29° 12′ 38″	29° 12′ 34″	29° 12′ 32″	29° 12′ 31″	29° 12′ 35″	29° 09′ 56″	29° 10′ 58″	29° 10′ 58″	29° 10′ 39″
SiO_2	56.03	53.99	56.05	59.56	56.4	55.74	56.9	57.34	55.05	55.68	57.95
TiO_2	0.69	0.78	0.84	0.67	0.79	0.75	0.77	0.74	0.86	0.83	0.85
Al_2O_3	17.56	18.1	17.6	17.76	18.18	17.9	17.74	18.55	16.79	18.01	21.09
$Fe_2O_3^*$	8.03	8.91	7.89	6.21	7.2	7.79	7.53	8.07	9.16	8.47	5.5
MnO	0.12	0.13	0.15	0.1	0.12	0.12	0.12	0.11	0.13	0.12	0.06
MgO	3.58	3.98	4.32	3.19	3.81	3.85	3.6	3	4.54	3.81	1.31
CaO	7.59	7.81	7.4	6.94	7.5	7.61	7.32	6.82	7.58	7.28	6.87
Na_2O	3.46	3.16	3.15	3.39	3.36	3.57	3.82	3.36	3.13	3.3	5.17
K_2O	1.41	1.01	1.41	1.16	0.92	1.01	0.78	1.15	1.54	1.4	0.36
P_2O_5	0.14	0.11	0.27	0.21	0.2	0.23	0.23	0.17	0.16	0.17	0.15
LOI	1.08	1.7	0.61	0.57	1.25	1.14	0.91	0.42	0.73	0.65	0.46
Total	99.71	99.69	99.69	99.75	99.74	99.7	99.72	99.74	99.68	99.72	99.77
Mg#	50.98	51.02	56.07	54.48	55.24	53.50	52.73	46.40	53.62	51.17	35.73
A/CNK	0.84	0.88	0.87	0.91	0.90	0.86	0.87	0.97	0.82	0.89	0.99
Sc	17.1	18.4	15.8	12.9	15.1	16.4	13.7	13.9	22.8	17.4	6.8
V	172	213	143	123	141	4175	4254	4004	5067	4640	4801
Cr	18.8	22.8	95.5	40.5	57.2	49.5	38.7	7.91	79.7	33.0	9.91
Co	44.9	58.7	45.6	52.1	54.0	927	967	835	1071	898	467
Ni	16.0	22.2	44.1	23.7	31.6	26.8	26.6	9.41	30.5	19.5	6.49
Ga	17.0	18.8	17.7	16.8	18.1	28.0	42.6	50.6	36.7	31.0	8.74
Ge	1.13	1.22	1.34	0.989	1.12	1.18	1.15	1.03	1.27	1.18	0.712
Rb	30.5	21.7	25.8	22.7	16.5	14.2	8.57	21.3	42.8	37.1	3.05
Sr	479	551	498	592	606	571	644	516	456	509	907
Y	14.9	14.0	18.3	13.0	15.1	16.5	12.3	18.5	16.1	14.9	6.54
Zr	7.38	26.0	32.7	36.3	29.4	30.1	31.8	57.9	39.4	55.6	8.92
Nb	2.56	1.68	5.53	3.67	3.89	3.83	3.15	2.70	3.55	3.79	2.48
Cs	2.26	1.79	0.852	0.335	0.360	0.224	0.273	1.65	2.17	2.24	0.317
Ba	267	217	218	279	253	210	191	187	353	281	108
La	9.88	7.96	13.9	11.0	11.7	11.9	10.8	9.46	12.5	13.2	7.15
Ce	23.0	17.8	33.3	24.3	26.7	28.1	23.8	22.2	27.9	28.6	14.3
Pr	3.04	2.46	4.52	3.21	3.81	3.88	3.30	3.29	3.72	3.70	1.78
Nd	12.6	10.5	19.0	13.2	15.6	15.7	13.7	14.4	15.1	15.1	6.95
Sm	2.79	2.44	3.92	2.76	3.32	3.30	2.92	3.45	3.39	3.23	1.43
Eu	0.772	0.923	1.13	0.941	1.07	1.06	1.00	0.951	1.03	1.03	0.635
Gd	2.61	2.40	3.76	2.58	3.08	3.14	2.75	3.52	3.28	3.05	1.37
Tb	0.443	0.417	0.574	0.406	0.504	0.507	0.422	0.598	0.536	0.490	0.208
Dy	2.61	2.44	3.26	2.40	2.88	2.94	2.32	3.48	3.01	2.68	1.19
Ho	0.536	0.508	0.647	0.476	0.566	0.600	0.467	0.684	0.607	0.543	0.242
Er	1.49	1.38	1.78	1.29	1.52	1.62	1.26	1.81	1.61	1.43	0.637
Tm	0.213	0.199	0.265	0.186	0.219	0.237	0.176	0.252	0.222	0.209	0.0870
Yb	1.42	1.33	1.70	1.21	1.38	1.51	1.16	1.58	1.46	1.34	0.579
Lu	0.221	0.218	0.255	0.190	0.222	0.245	0.185	0.246	0.229	0.205	0.0920
Hf	0.392	0.835	1.04	0.976	0.899	0.880	0.890	1.586	1.082	1.42	0.347
Ta	0.261	0.208	0.326	0.339	0.279	0.252	0.217	0.278	0.320	0.331	0.346
Pb	10.7	7.73	4.75	4.59	3.68	4.54	4.51	9.08	7.25	7.97	9.49
Th	2.30	1.90	1.24	0.464	0.208	0.203	0.442	1.19	2.01	2.70	0.724
U	0.885	0.603	0.132	0.0920	0.0650	0.0800	0.226	0.479	0.509	0.712	0.360
Sr/Y	32.15	39.36	27.21	45.54	40.13	34.61	52.36	27.89	28.32	34.16	138.69
La/Yb	6.96	5.98	8.18	9.09	8.48	7.88	9.31	5.99	8.56	9.85	12.33
Eu*/Eu	0.87	1.16	0.90	1.08	1.02	1.01	1.08	0.83	0.94	1.00	1.40

Sample	09TB47-3	09TB50	09TB51-1	09TB51-2	09TB36	09TB38-2	09TB41-1	09TB45-1	09TB45-2	09TB48-1
Rock type	Diorite	Diorite	Diorite	Diorite	Granodiorite	Granodiorite	Granodiorite	Granodiorite	Granodiorite	Granodiorite
Longitude	93° 56′ 00″	93° 52′ 12″	93° 50′ 10″	93° 50′ 10″	94° 04′ 34″	94° 03′ 33″	94° 03′ 15″	94° 04′ 33″	93° 59′ 22″	93° 54′ 48″
Latitude	29° 10′ 39″	29° 07′ 06″	29° 07′ 24″	29° 07′ 24″	29° 12′ 41″	29° 12′ 38″	29° 12′ 31″	29° 11′ 50″	29° 09′ 56″	29° 09′ 47″
SiO_2	54.51	57.91	55.31	53.91	62.47	63.18	64.09	64.39	65.74	63.67
TiO_2	0.94	0.68	0.78	0.81	0.64	0.58	0.54	0.55	0.48	0.54
Al_2O_3	17.07	17.06	18.32	18.50	16.73	17.01	17.53	16.36	16.47	16.46
$Fe_2O_3^*$	9.78	7.07	8.74	9.66	5.74	5.21	4.81	5.66	4.9	5.81
MnO	0.14	0.11	0.13	0.16	0.10	0.10	0.07	0.10	0.08	0.08
MgO	4.17	2.96	3.58	3.92	2.74	2.38	2.24	2.38	2.01	2.23
CaO	7.45	6.40	7.64	8.06	5.66	5.72	5.29	5.03	4.26	5.30
Na_2O	3.39	4.83	3.22	3.24	3.15	3.23	3.16	3.35	3.31	3.65
K_2O	1.42	1.67	0.90	0.91	1.61	1.55	0.98	1.48	2.08	1.40
P_2O_5	0.21	0.17	0.18	0.21	0.20	0.18	0.17	0.12	0.11	0.13
LOI	0.58	0.88	0.90	0.30	0.73	0.64	1.01	0.39	0.37	0.50
Total	99.67	99.73	99.7	99.67	99.78	99.78	99.88	99.79	99.81	99.77
Mg#	49.82	49.41	48.82	48.6	52.67	51.58	52.05	49.52	48.9	47.25

Table 2 (continued)

Sample	09TB47-3	09TB50	09TB51-1	09TB51-2	09TB36	09TB38-2	09TB41-1	09TB45-1	09TB45-2	09TB48-1
Rock type	Diorite	Diorite	Diorite	Diorite	Granodiorite	Granodiorite	Granodiorite	Granodiorite	Granodiorite	Granodiorite
Longitude	93° 56′ 00″	93° 52′ 12″	93° 50′ 10″	93° 50′ 10″	94° 04′ 34″	94° 03′ 33″	94° 03′ 15″	94° 04′ 33″	93° 59′ 22″	93° 54′ 48″
Latitude	29° 10′ 39″	29° 07′ 06″	29° 07′ 24″	29° 07′ 24″	29° 12′ 41″	29° 12′ 38″	29° 12′ 31″	29° 11′ 50″	29° 09′ 56″	29° 09′ 47″
A/CNK	0.83	0.80	0.91	0.88	0.97	0.98	1.10	1.01	1.07	0.96
Sc	19.8	14.3	19.0	17.8	10.1	8.48	8.12	10.7	9.03	8.01
V	4901	3845	4402	4636	115	95.1	87.3	3094	2810	3046
Cr	27.7	9.52	5.17	3.50	37.9	24.0	28.0	10.3	10.0	13.9
Co	1028	854	1035	1174	55.3	45.2	57.2	720	698	644
Ni	18.0	12.5	11.8	11.5	21.6	16.4	16.1	8.73	8.98	10.2
Ga	45.8	47.3	71.2	57.1	16.9	15.0	15.7	6.83	30.6	4.94
Ge	1.22	1.19	1.15	1.20	1.15	1.02	1.01	1.22	1.19	1.03
Rb	28.0	41.6	18.0	17.5	35.2	29.2	21.0	38.8	46.4	29.5
Sr	468	480	514	560	511	517	598	380	387	495
Y	16.4	13.6	14.5	11.1	11.8	10.0	8.77	10.1	9.60	9.05
Zr	21.0	46.1	34.4	23.5	54.6	26.4	45.2	32.0	67.2	30.2
Nb	3.46	2.96	2.82	2.56	4.86	3.76	2.86	2.64	2.52	1.88
Cs	1.77	2.05	1.38	1.64	0.656	0.425	0.426	1.32	0.651	1.01
Ba	269	312	215	212	287	399	258	239	409	349
La	12.4	11.0	10.4	10.0	13.9	12.5	11.5	10.3	11.7	10.3
Ce	28.0	24.1	23.2	21.6	29.5	25.4	22.4	20.7	23.3	20.8
Pr	3.80	3.15	3.06	2.71	3.76	3.28	2.85	2.60	2.83	2.61
Nd	15.4	12.8	12.4	10.6	14.4	12.8	10.5	10.0	10.6	10.0
Sm	3.35	2.78	2.69	2.12	2.84	2.55	2.03	2.01	2.02	2.00
Eu	0.949	0.818	0.913	0.877	0.947	0.902	0.784	0.636	0.686	0.764
Gd	3.21	2.65	2.75	2.05	2.62	2.28	1.91	1.91	1.90	1.95
Tb	0.518	0.416	0.443	0.342	0.396	0.351	0.285	0.303	0.300	0.301
Dy	2.96	2.45	2.59	1.94	2.22	1.97	1.63	1.72	1.68	1.61
Ho	0.594	0.499	0.531	0.408	0.444	0.395	0.328	0.363	0.357	0.329
Er	1.62	1.33	1.49	1.09	1.20	1.02	0.843	1.02	1.01	0.871
Tm	0.236	0.196	0.208	0.156	0.170	0.149	0.121	0.152	0.146	0.142
Yb	1.43	1.25	1.41	1.07	1.13	0.966	0.788	1.01	1.00	0.849
Lu	0.227	0.193	0.234	0.177	0.172	0.153	0.115	0.170	0.173	0.132
Hf	0.635	1.17	0.980	0.683	1.36	0.710	1.13	0.881	1.95	0.829
Ta	0.303	0.277	0.315	0.348	0.432	0.329	0.309	0.317	0.317	0.262
Pb	7.60	9.25	8.11	6.80	5.56	5.85	4.36	8.63	11.0	6.39
Th	1.91	1.03	2.40	2.05	0.875	0.230	0.239	1.72	2.39	1.29
U	0.515	0.289	0.676	0.569	0.205	0.0850	0.0880	0.638	0.640	0.407
Sr/Y	28.54	35.29	35.45	50.45	43.31	51.70	68.19	37.62	40.31	54.70
La/Yb	8.67	8.80	7.38	9.35	12.30	12.89	14.56	10.20	11.70	12.12
Eu*/Eu	0.89	0.92	1.02	1.29	1.06	1.14	1.21	1.00	1.08	1.18

$Fe_2O_3^*$ = Total Fe_2O_3 content; $Mg^\# = Mg^{2+} / (Mg^{2+} + Fe^{2+}) * 100$; $\delta Eu = Eu_N / (Sm_N \times Gd_N)^{1/2}$.

Zr–Hf–Ti anomalies) (e.g., Ji et al., 2009a; Ma et al., 2013-a,b; Wen et al., 2008a,b). In summary, geological evidence overwhelmingly suggests that the Milin adakitic charnockites were generated in an arc setting.

5.2. Petrogenesis

As noted above, the Milin charnockites have adakitic affinities, e.g., high SiO_2, Sr contents, Sr/Y and La/Yb ratios and low Y and Yb contents (Fig. 4d). It is now widely recognized that adakitic rocks may be generated by a variety of mechanisms (Castillo, 2006, 2012), such as melting of subducted young and hot oceanic crust (Defant and Drummond, 1990), partial melting of thickened basaltic lower crust (Atherton and Petford, 1993; Kay and Kay, 1993; Wen et al., 2008b), partial melting of subducted continental crust (Wang et al., 2008), crustal assimilation and low-pressure fractional crystallization from parental basaltic magmas (Castillo et al., 1999; Li et al., 2009), high-pressure crystallization (involving garnet) of mafic magmas derived from mantle wedge peridotites (Macpherson et al., 2006), and magma mixing between felsic and basaltic magmas (Streck et al., 2007). We consider these alternative processes in the following sections with specific reference to the Milin adakitic charnockites.

First, the Milin adakitic charnockites could not be generated by high- or low pressure crystallization from parental basaltic magmas. Given that high-pressure crystallization involving garnet will cause a decrease in HREE and Y contents, the Sr/Y and Dy/Yb ratios in the residual magmas will increase with increasing SiO_2 contents (Davidson et al., 2007; Macpherson et al., 2006). However, the Milin adakitic rocks do not show such trends in their chondrite-normalized rare earth element patterns (Fig. 5a) or on Sr/Y and Dy/Yb vs. SiO_2 diagrams (Fig. 8c–d). During low-pressure fractional crystallization involving olivine and pyroxene, the derived magmas should show a clear decrease in $Mg^\#$ values as well as Cr and Ni contents with the increasing SiO_2 contents (Castillo et al., 1999), but the $Mg^\#$ values of the Milin adakitic charnockites are relatively constant (Fig. 4f). The decrease of MgO and FeO contents with increasing SiO_2 suggest that the Milin adakitic rocks probably underwent amphibole fractionation. However, amphibole fractionation is seldom isolated and is typically accompanied by plagioclase removal in natural systems (Moyen, 2009), and the net effect of amphibole and plagioclase fractionation is an increase in La/Yb, decrease in Dy/Yb, and moderate increase or even decrease in Sr/Y, which is observed in most arc adakites (Moyen, 2009). In addition, although amphibole is rather efficient in changing the trace element budget, the amount of amphibole that can be formed is limited by the Fe and Mg budget to a small mass fraction (in the region of 20%), strongly reducing its potential effect (Moyen, 2009). The modeling calculation for the similar Archean TTGs also indicates that this sort of fractionation is apparently not enough to evolve a non-adakitic suite into an adakitic one (Moyen et al., 2007). Therefore, amphibole + plagioclase fractionation can contribute to the geochemical trends observed, but has little or no potential to actually yield adakitic signatures in the first place (Moyen, 2009).
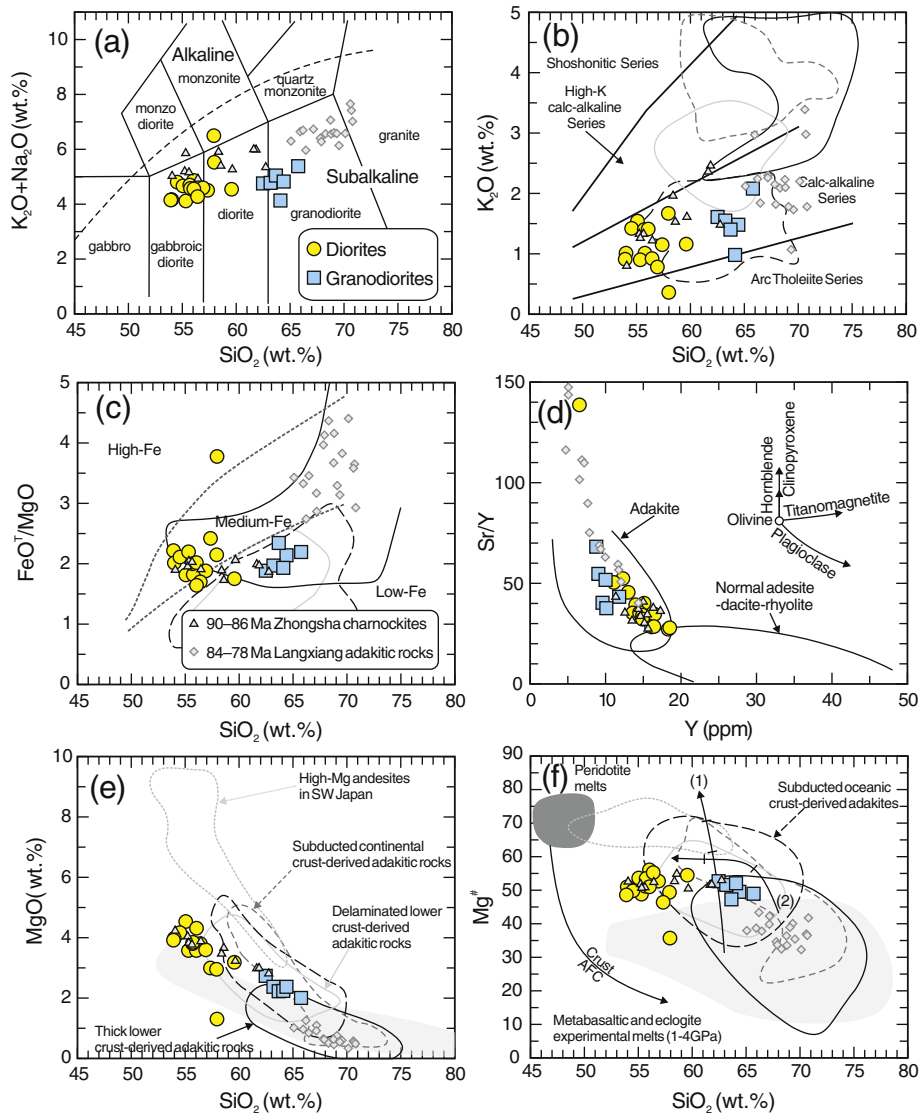
Fig. 4. (a) SiO_2–$K_2O + Na_2O$ plot (Middlemost, 1994). (b) SiO_2–K_2O plot (Peccerillo and Taylor, 1976). (c) SiO_2 versus FeO^T/MgO diagrams (Miyashiro, 1974). Boundaries (gray lines) between low-, medium-, and high-Fe suites are after Arculus (2003). (d) Y versus Sr/Y (after Defant and Drummond, 1993). Crystal fractionation paths of the primary minerals are from Castillo et al. (1999). (e) SiO_2 versus MgO diagram. (f) SiO_2 versus $Mg^\#$ diagram. Mantle AFC curves, with proportions of assimilated peridotite indicated, are after Stern and Kilian (1996) (Curve 1) and Rapp et al. (1999) (Curve 2), peridotite melts and crust AFC curves from Stern and Kilian (1996). Data for metabasalt and eclogite experimental melts (1–4.0 GPa), and peridotite-hybridized equivalents, are from Rapp et al. (1999) and references therein. Data for high-Mg andesites of SW Japan are from the following references: Shimoda et al. (1998), Tatsumi et al. (2006), Tatsumi et al. (2006), and references therein. Data for the 84–78 Ma Langxian adakitic rocks are from Guan et al. (2010) and Wen et al. (2008a). Data for the 90–86 Ma Zhongsha charnockites are from Zhang et al. (2012). The fields of subducted oceanic crust-, delaminated lower crust-, and thickened lower crust-derived adakites are after Wang et al. (2006).

Second, it is also unlikely that magma mixing between felsic and basaltic magmas produced the Milin adakitic charnockites. The magma mixing model generally needs mantle-derived basaltic and crust-derived felsic end-members (e.g., Streck et al., 2007). In the Milin area, candidates for mantle-derived basaltic and crust-derived felsic end-members are most plausibly represented by the 95–90 Ma Gangdese mafic intrusive rocks (Guan et al., 2011; Ma et al., 2013-a,b) and the 84–78 Ma Langxian adakitic granites derived by melting of thickened continent crust (Guan et al., 2010; Wen et al., 2008b), respectively. However, some Milin adakitic granodiorite samples (e.g., 09TB45-1, 09TB45-2 and 09TB48-1) with the highest SiO_2 contents have the highest $\varepsilon_{Nd}(t)$ and $\varepsilon_{Hf}(t)$ values. Their $\varepsilon_{Hf}(t)$ values are higher than those of the reported coeval basaltic and felsic endmembers (Figs. 4f, 6 and 8), which are inconsistent with the magma mixing model (e.g., Streck et al., 2007). In addition, the diorites and granodiorites with variable SiO_2 (54 to 66 wt.%) contents have approximately constant Sr–

Nd–Hf isotopic compositions (Fig. 6), which are also inconsistent with the model of magma mixing.

Third, the Milin adakitic charnockites could not have been generated by partial melting of thickened, delaminated or subducted continental lower crust. Thickened continental lower crust-derived adakitic rocks occur widely in southern Tibet (e.g., Chung et al., 2003, 2009; Guan et al., 2012; Guo et al., 2007; Hou et al., 2004; Ji et al., 2012; Wen et al., 2008a). For instance, the Late Cretaceous (84–78 Ma) Langxian adakitic rocks derived from thickened lower crust (Wen et al., 2008a) are slightly younger than the ~90 Ma Milin adakitic charnockites. Commonly, adakitic rocks derived from thickened lower crust are characterized by relatively low MgO or $Mg^\#$ values similar to those of experimental melts from metabasalts and eclogites (Rapp and Watson, 1995; Rapp et al., 1999; Sen and Dunn, 1994). Previous studies also showed that adakitic rocks generated by melting of thickened lower crust have lower MgO, HREE, Y contents and higher Sr/Y, $(La/Yb)_N$ and
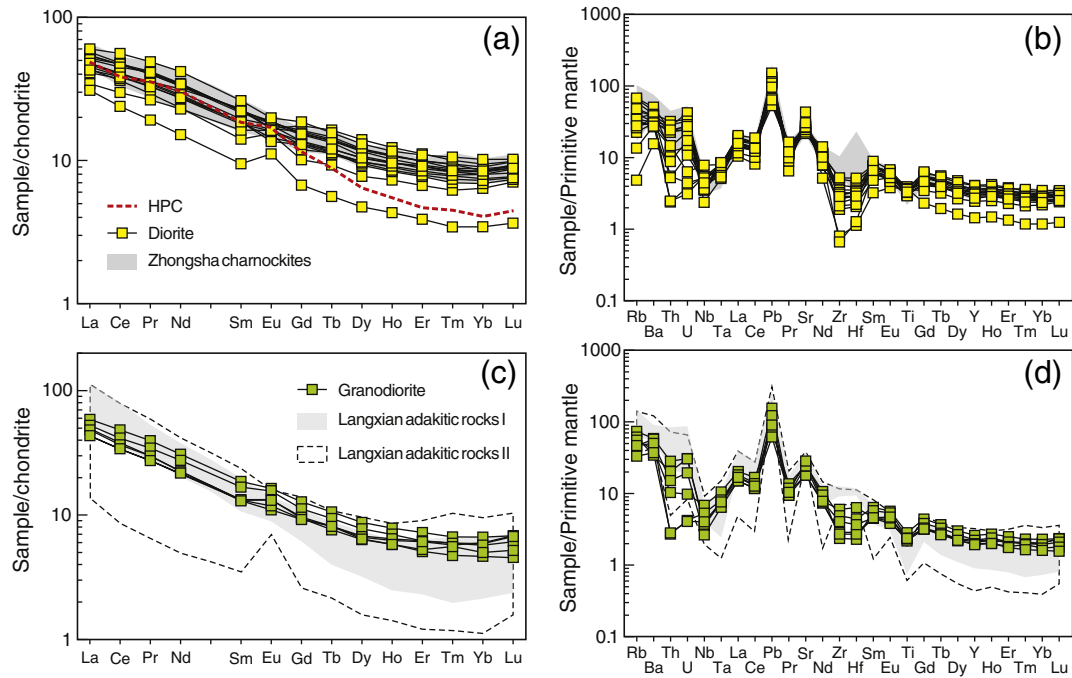
Fig. 5. Chondrite-normalized rare earth element (REE) patterns; (b) primitive mantle-normalized multi-element patterns of the Milin charnockitic diorites; (c) chondrite-normalized rare earth element (REE) patterns and (d) primitive mantle-normalized multi-element patterns of the Milin charnockitic granodiorites. The adakitic rock data derived by high-pressure crystallization (HPC) are from Macpherson et al. (2006). The data of Late Cretaceous (89–85 Ma) adakitic charnockites in the Zhongsha area are from Zhang et al. (2010a,b). The data of the Langxian adakitic rocks generated by partial melting of thickened mafic lower crust are from Guan et al. (2010) and Wen et al. (2008a,b). The trace element compositions of enriched middle oceanic ridge basalt (E-MORB) and normal middle oceanic ridge basalt (N-MORB), chondrite and primitive mantle normalization values are from Sun and McDonough (1989).

$(Dy/Yb)_N$ ratios than those of adakites derived from subducted oceanic slabs (e.g., Chen et al., 2011; Guan et al., 2012; Macpherson et al., 2006; Wang et al., 2006, 2007). Thus, the slightly higher MgO, HREE and Y contents, lower SiO_2 and K_2O contents, and lower Sr/Y, $(La/Yb)_N$ and $(Dy/Yb)_N$ ratios of the Milin adakitic charnockites are inconsistent with them being derived from thickened lower crust (Figs. 4 and 5). On the other hand, the Milin adakitic charnockites have $\varepsilon_{Nd}(t)$ values (+2.4 to +4.2) overlapping with those (+0.9 to +3.2 and −0.2 to +4.1) of Late Cretaceous thickened lower crust-derived adakitic rocks (Wen et al., 2008a) and mantle-derived mafic rocks in southern Tibet (Guan et al., 2011; Ma et al., in press-b) within analytical error, although

with slightly higher and more homogeneous $\varepsilon_{Nd}(t)$ values (Fig. 6c). Moreover, they also exhibit slightly higher and more homogeneous $\varepsilon_{Hf}(t)$ values (+12 to +16, corresponding to Indian Ocean MORB) than those of the Zhengga gabbros and Langxian adakitic rocks (+2.9 to +11.1 and +6.6 to +20.0, respectively) (Fig. 6c). They also have clearly lower Th (0.20–2.39 ppm) and Th/La (0.02–0.23) values and higher Mg# (46–56) than those (1.84–6.95 ppm, 0.14–0.32, 32–39) of the thickened lower crust-derived Langxian adakitic rocks (Fig. 9 and Table 2).

Overall, all lines of evidence indicate that the Milin charnockites are different from adakitic rocks derived from thickened lower crust, and

Table 3
Sr and Nd isotope data for the Milin granitoids.

Sample	Rock type	$^{87}Rb/^{86}Sr$	$^{87}Sr/^{86}Sr \pm 2\sigma$	$(^{87}Sr/^{86}Sr)_i$	$^{147}Sm/^{144}Nd$	$^{143}Nd/^{144}Nd \pm 2\sigma$	$(^{143}Nd/^{144}Nd)_i$	$\varepsilon_{Nd}(t)$	T_{DM} (Ma)
09TB21-2	Diorite	0.1844	0.704579 ± 12	0.704335	0.1342	0.512788 ± 6	0.512707	3.68	698
09TB22	Diorite	0.1138	0.704521 ± 12	0.704371	0.1410	0.512786 ± 6	0.512700	3.55	768
09TB38-1	Diorite	0.1495	0.704561 ± 12	0.704363	0.1246	0.512750 ± 6	0.512674	3.03	688
09TB39	Diorite	0.1108	0.704430 ± 11	0.704283	0.1270	0.512737 ± 6	0.512660	2.77	729
09TB41-3	Diorite	0.0720	0.704427 ± 11	0.704332	0.1269	0.512754 ± 7	0.512677	3.09	700
09TB45-3	Diorite	0.1191	0.704448 ± 11	0.704291	0.1444	0.512797 ± 6	0.512709	3.71	783
09TB46-2	Diorite	0.2109	0.704496 ± 12	0.704218	0.1294	0.512760 ± 6	0.512681	3.17	710
09TB47-1	Diorite	0.0097	0.704231 ± 14	0.704218	0.1241	0.512768 ± 8	0.512693	3.41	653
09TB47-3	Diorite	0.1730	0.704451 ± 12	0.704223	0.1316	0.512775 ± 5	0.512695	3.45	701
09TB50	Diorite	0.2501	0.704564 ± 14	0.704234	0.1307	0.512767 ± 7	0.512687	3.30	708
09TB51-2	Diorite	0.0904	0.704346 ± 14	0.704227	0.1203	0.512781 ± 13	0.512708	3.70	605
09TB36	Granodiorite	0.1992	0.704668 ± 14	0.704405	0.1194	0.512714 ± 6	0.512641	2.40	709
09TB38-2	Granodiorite	0.1632	0.704559 ± 13	0.704344	0.1201	0.512738 ± 6	0.512665	2.87	674
09TB41-1	Granodiorite	0.1017	0.704411 ± 10	0.704277	0.1168	0.512738 ± 7	0.512667	2.89	652
09TB45-1	Granodiorite	0.2954	0.704592 ± 12	0.704202	0.1214	0.512794 ± 7	0.512720	3.94	591
09TB45-2	Granodiorite	0.3472	0.704645 ± 11	0.704187	0.1157	0.512796 ± 7	0.512725	4.04	555
09TB48-1	Granodiorite	0.1727	0.704475 ± 13	0.704247	0.1203	0.512790 ± 7	0.512717	3.88	591

$^{87}Rb/^{86}Sr$ and $^{147}Sm/^{144}Nd$ are calculated using whole-rock Rb, Sr, Sm and Nd contents in Table 3.
$\varepsilon_{Nd}(t) = [(^{143}Nd/^{144}Nd)_{sample}/(^{143}Nd/^{144}Nd)_{CHUR} - 1] \times 10000$. $T_{DM} = ln[(^{143}Nd/^{144}Nd)_{sample} - (^{143}Nd/^{144}Nd)_{DM}]/[(^{147}Sm/^{144}Nd)_{sample} - (^{147}Sm/^{144}Nd)_{DM}]/\lambda$ (DePaolo, 1988).
In the calculation, $(^{143}Nd/^{144}Nd)_{CHUR} = 0.512638$, $(^{147}Sm/^{144}Nd)_{CHUR} = 0.1967$, $(^{143}Nd/^{144}Nd)_{DM} = 0\cdot51315$, $(^{147}Sm/^{144}Nd)_{DM} = 0\cdot2136$ and t = 92.8 Ma.
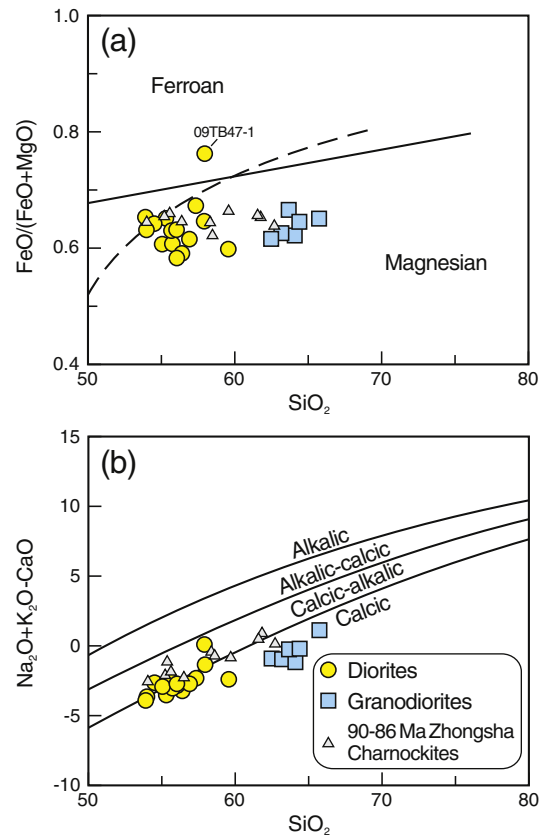
Fig. 7. Classification diagrams for the charnockites (after Frost and Frost (2008)). (a) FeO / (FeO + MgO) versus SiO$_2$ plot and (b) Na$_2$O + K$_2$O–CaO versus SiO$_2$. The data of Zhongsha charnockites are from Zhang et al. (2010a).

Th/La = 0.15–0.71) of high-K calc-alkaline adakitic rocks derived from subducted continental crust (Wang et al., 2008) or delaminated continental lower crust (e.g., Wang et al., 2006; Xu et al., 2002).

We suggest that the Milin adakitic charnockites were most probably generated by partial melting of subducted Neo-Tethyan oceanic crust. All the Milin adakitic charnockites have higher SiO$_2$ (54 to 66 wt.%) contents (Table 2). Apart from one diorite sample (09 TB47-1) with the lowest Mg$^{\#}$ (35.7) and MgO (1.31 wt.%), the diorite and granodiorite samples have high Mg$^{\#}$ (46.4 to 56.1) values and MgO (2.01 to 4.54 wt.%) contents similar to those of slab-derived adakitic melts (Mg$^{\#}$ > ~47; Martin, 1999; Smithies, 2000), indicating that the magmas interacted with the mantle wedge peridotites during ascent. In addition, the Milin adakitic magmatic rocks have depleted Nd isotope compositions ($\varepsilon_{Nd}(t)$ = +2.4 to +4.0) (Table 3) comparable to those of the Tethyan basalts ($\varepsilon_{Nd}(t)$ = +3.01 to +12.3; e.g., Mahoney et al., 1998; Xu and Castillo, 2004; Zhang et al., 2005) (Fig. 6a). Their higher Hf isotope compositions ($\varepsilon_{Hf}(t)_{zircon}$ = +10.1 to +15.8) (Supplementary File 2) are also similar to those of Indian Ocean MORB (Ingle et al., 2003). The slightly higher MgO, HREE and Y contents and lower SiO$_2$, K$_2$O and Th contents and Sr/Y, Th/La, (La/Yb)$_N$ and (Dy/Yb)$_N$ ratios of the Milin adakitic charnockites are consistent with those of adakites derived from subducted oceanic crust (e.g., Chen et al., 2011; Guan et al., 2012; Macpherson et al., 2006; Wang et al., 2006, 2007) (Figs. 4, 5 and 9). In addition, they have low Th and Th/La values similar to those of typical MORB (Fig. 9a), indicating that they contain a main component from subducted basaltic oceanic crust (Wang et al., 2006, 2007, 2008). Therefore, all evidence suggests that they were probably derived from partial melting of subducted oceanic crust. In addition, their primitive-mantle-normalized trace element patterns are comparable to high SiO$_2$ adakite (HSA) (Martin et al., 2005) and typical adakites as defined by Defant et al. (1991) (Fig. 10).
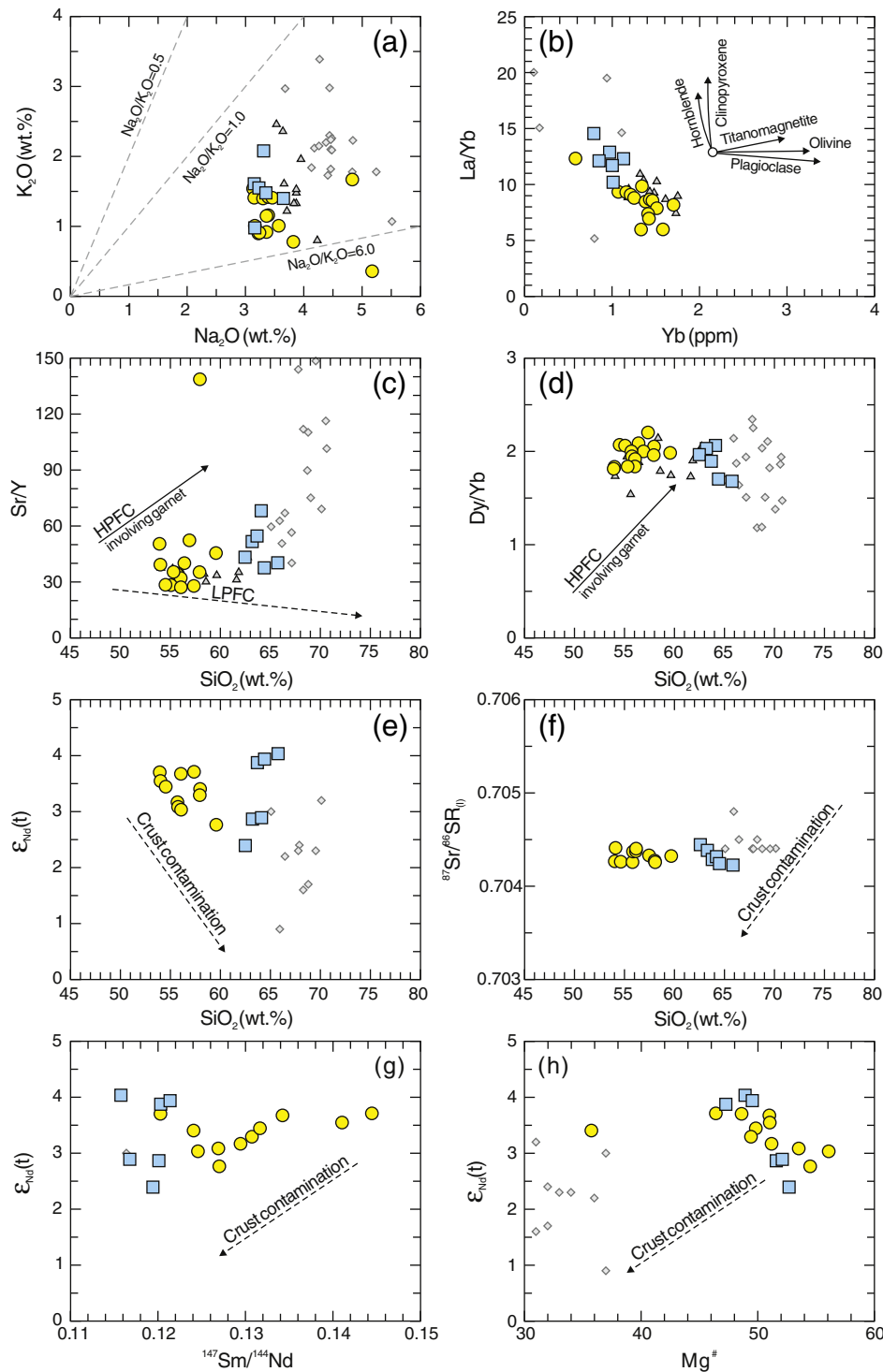

Fig. 6. (a) $\varepsilon_{Nd}(t)$ vs. (^{87}Sr/^{86}Sr)$_i$ (enlarged diagram in inset); (b) $\varepsilon_{Hf}(t)$ vs. U–Pb age diagrams for zircon in the Milin charnockites; (c) zircon $\varepsilon_{Hf}(t)$ vs. $\varepsilon_{Nd}(t)$ diagrams for the Milin charnockites. Data sources: Neo-Tethyan ophiolites are from the Indus–Yarlung Suture Zone (IYSZ) (Mahoney et al., 1998; Xu and Castillo, 2004; Zhang et al., 2005) and a gneiss sample representing the upper crust (Nd = 31.96 ppm, ε_{Nd}(t = 92.8 Ma) = −10.58, Sr = 130.0 ppm, (^{87}Sr/^{86}Sr)$_i$ = 0.7520, Ma et al., in press-b); lower crustal data ($\varepsilon_{Nd}(t)$ = −10.2, (^{87}Sr/^{86}Sr)$_i$ = 0.7044, Nd = 11 ppm, Sr = 348 ppm) are from Wen (2007) except that the Sr and Nd concentrations are assumed values from Rudnick and Gao (2003). The data of Zhengga mafic rocks and the Langxian adakitic rocks are from Chu et al. (2011), Ma et al. (2013-a) and Wen et al. (2008a), respectively. The data of Late Cretaceous (ca. 93 Ma) Milin mafic rocks are from Ma et al. (2013-a). The Gangdese and Ladakh batholith Hf isotope composition fields are constructed by the data from Ji et al. (2009a) and Ravikant et al. (2009), respectively. Field of Hf–Nd isotopic data for Indian MORB, OIB and mantle array are from Chauvel and Blichert-Toft (2001) and Ingle et al. (2003).

could not have originated from a thickened mafic lower crust. In addition, their geochemical characteristics (Figs. 4b and 6a, Table 2) also do not match those ($\varepsilon_{Nd}(t)$ < −3.0; K$_2$O > 3.0 wt.%; Th = 8.0–30.4 ppm;

Fig. 8. (a) Na$_2$O versus K$_2$O; (b) Yb versus La/Yb, crystal fractionation paths of the primary minerals are from Castillo et al. (1999); (c) SiO$_2$ versus Sr/Y; (d) SiO$_2$ versus Dy/Yb; (e) SiO$_2$ versus ε$_{Nd}$(t); and (f) SiO$_2$ versus (^{87}Sr/^{86}Sr)$_i$ plots; (g) ^{147}Sm/^{144}Nd versus ε$_{Nd}$(t); (e) Mg$^#$ versus ε$_{Nd}$(t). HPFC, high-pressure fractional crystallization involving garnet (Macpherson et al., 2006); LPFC: crystal fractionation of an island arc tholeiite series basalt (Danyushevsky et al., 2008). Data sources and symbols are the same as in Fig. 4.

On the discrimination diagrams for low-SiO$_2$-adakites (LSAs) and high-SiO$_2$-adakites (HSAs) (Fig. 11), the Milin adakitic samples mainly plot in the field of HSAs derived from interactions between slab-derived melts and mantle peridotites (e.g., Martin et al., 2005; Rapp et al., 1999). Their relatively variable ε$_{Nd}$(t) values and correlations between SiO$_2$ contents and ^{147}Sm/^{144}Nd ratios or ε$_{Nd}$(t) values (Fig. 8e and g) suggest that minor crustal contamination may have occurred during the formation of some Milin adakitic rocks. However, the relatively uniform initial ^{87}Sr/^{86}Sr ratios and negative correlations between Mg$^#$ and ε$_{Nd}$(t)

values are inconsistent with extensive crustal contamination. Thus, we suggest that the Milin adakitic rocks likely underwent a two-stage contamination-evolution process: 1) slab-derived melts were first contaminated by mantle peridotite during melt ascent, which increased their MgO and compatible elements contents (Fig. 4e); and 2) the melts then underwent minor contamination with assimilated metamorphic basement rock and fractional crystallization of amphibole + plagioclase during passage through the crust. In this study, three adakitic granodiorite samples (09TB45-1, 09TB45-2 and 09TB48-1) with higher ε$_{Nd}$(t)
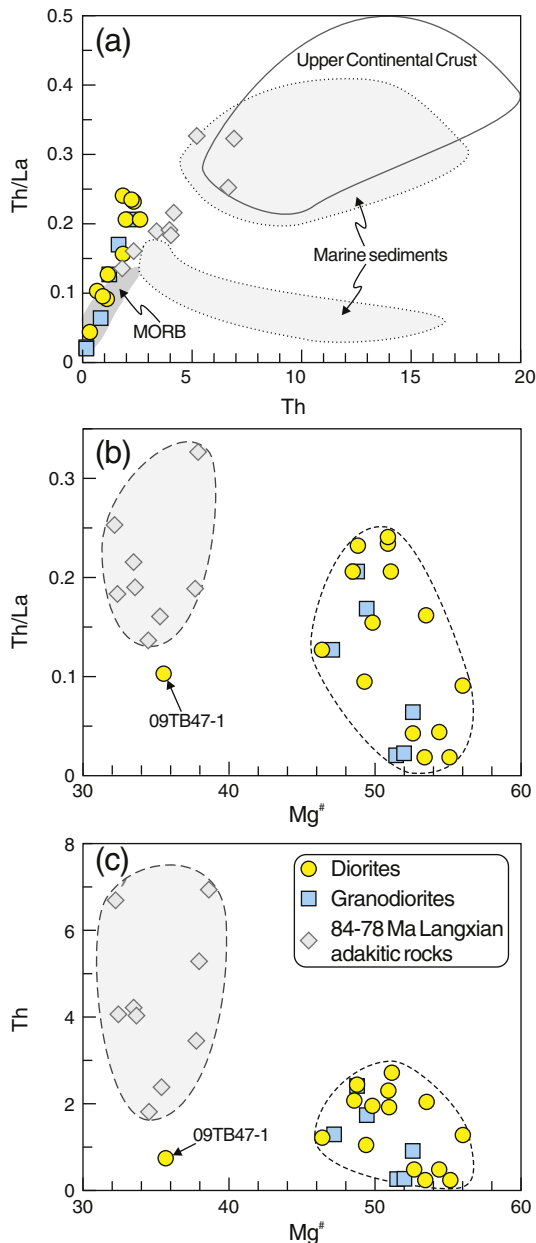
Fig. 9. (a) Th versus Th/La, (b) Mg# versus Th/La and (c) Mg# versus Th diagram. The data for upper continental crust are from Plank (2005) and references therein. The data for marine sediments are from Plank and Langmuir (1998). MORB data are from Niu and Batiza (1997). The data for Langxian adakitic rocks are from Wen et al. (2008a).
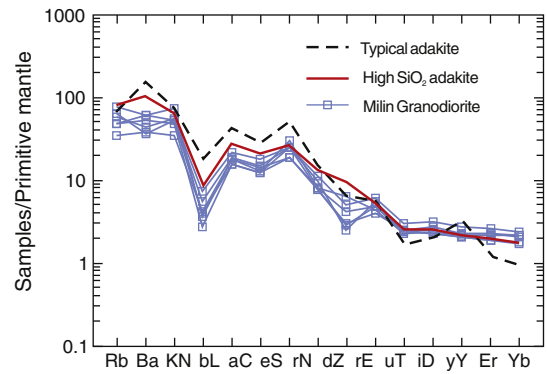

Fig. 10. Primitive-mantle-normalized trace element patterns of the Milin charnockitic granodiorites. The data of high SiO_2 adakite (HSA) and typical adakite are from Martin et al. (2005) and Defant et al. (1991), respectively.

($+3.9$–$+4.0$) and $\varepsilon_{Hf}(t)$ ($+12.8$–$+15.8$) values were probably directly from subducted oceanic slab, whereas the other three adakitic granodiorite samples with lower $\varepsilon_{Nd}(t)$ ($+2.4$–$+2.9$) and $\varepsilon_{Hf}(t)$ ($+10.6$–$+12.2$) values possibly underwent minor crustal contamination or had a minor sedimentary contribution (Fig. 6; Table 3). The Milin adakitic diorites with high MgO contents (3.0–4.5 wt.%) were probably generated by interactions between slab-derived melts and mantle peridotite (Fig. 6).

5.3. Geodynamic processes and implications for continental crustal growth

5.3.1. Geodynamic processes

Zircon U–Pb dating results indicate that a Late Cretaceous (ca. 100–80 Ma) magmatic "flare up" occurred in the southern Lhasa block (e.g., Ji et al., 2009a; Ma et al., 2013-a; Wen et al., 2008b). Various geodynamic models have been proposed for this magmatic event,

such as normal-angle subduction (100–85 Ma) and subsequent low-angle or flat-slab subduction (85–80 Ma) (e.g., Wen et al., 2008a), oceanic ridge subduction (e.g., Guan et al., 2010; Zhang et al., 2010b) and roll-back of subducted slab (e.g., Ma et al., 2013-a). All these processes have the potential to generate the adakites (e.g., Defant and Drummond, 1990; Guivel et al., 2003; Gutscher et al., 2000; Kay et al., 1993; Tang et al., 2012; Yogodzinski et al., 1995).

The early Late Cretaceous mafic magmas (e.g., Guan et al., 2011; Ma et al., 2013-a,b; Wen et al., 2008b) and adakites (e.g., Jiang et al., 2012; Kang et al., 2010; Zhang et al., 2010a and this study) found in the region are consistent with the mid-ocean ridge subduction model in some aspects, given that the rocks indicate high temperatures and require mantle contributions that could be attributed to mantle upwelling through a slab window (Thorkelson and Breitsprecher, 2005; Sisson et al., 2003). If the mid-ocean ridge subduction model is correct, the lack of any age trend in the distribution of mafic rocks and adakites (Fig. 1c; e.g., Guan et al., 2011; Jiang et al., 2012; Kang et al., 2010; Ma et al., 2013-a,b; Wen et al., 2008b; Zhang et al., 2010a and this study) would imply a spreading ridge sub-parallel to the trench. However, the subduction of a spreading ridge that is sub-parallel to the trench is likely to cease because of the dominance of young buoyant oceanic crust (e.g., Thorkelson, 1996), rather than lasting for over 15 Ma.

Although the ca. 100–85 Ma "normal-angle" subduction model (Wen et al., 2008a) can account for the magmatism over a wide area, partial melting of subducted oceanic crust occurs only under a restricted set of circumstances (800–1000 °C at depths of 70–80 km, Peacock et al., 1994; Sen and Dunn, 1994). A simple normal-angle subduction model does not explain the occurrence of the Milin adakitic rocks and the restriction of a contemporary magmatic "flare-up" to only the Gangdese sector of the southern Lhasa block (Ma et al., 2013-a).

We therefore prefer a model where subduction of Neo-Tethyan oceanic lithosphere occurred at low-angle up to the early Late Cretaceous as discussed in detail in Ma et al. (2013-a). If slab roll-back began at this time, then it can readily account for the contemporary Gangdese magmatic "flare-up" and subsequent underplating of mafic magmas based on the following evidence.

Late Jurassic–Early Cretaceous magmatic rocks occur widely in the central and northern Lhasa sub-block (Zhu et al., 2008, 2009a,b, 2011, 2012), whereas contemporaneous magmatic rocks only occur sporadically in the southern Lhasa sub-block (Wen et al., 2008a), suggesting that the magmatic front moved further north due to flat or low-angle subduction in the Early Cretaceous (Fig. 12) (Coulon et al., 1986; Kapp et al., 2005; Zhang et al., 2004, 2012). In our recent study, we reported on the high-temperature (up to 1340 °C) norites in the Milin area, which originated from asthenosphere–lithosphere interactions due to the asthenospheric upwelling as a result of the roll-back of
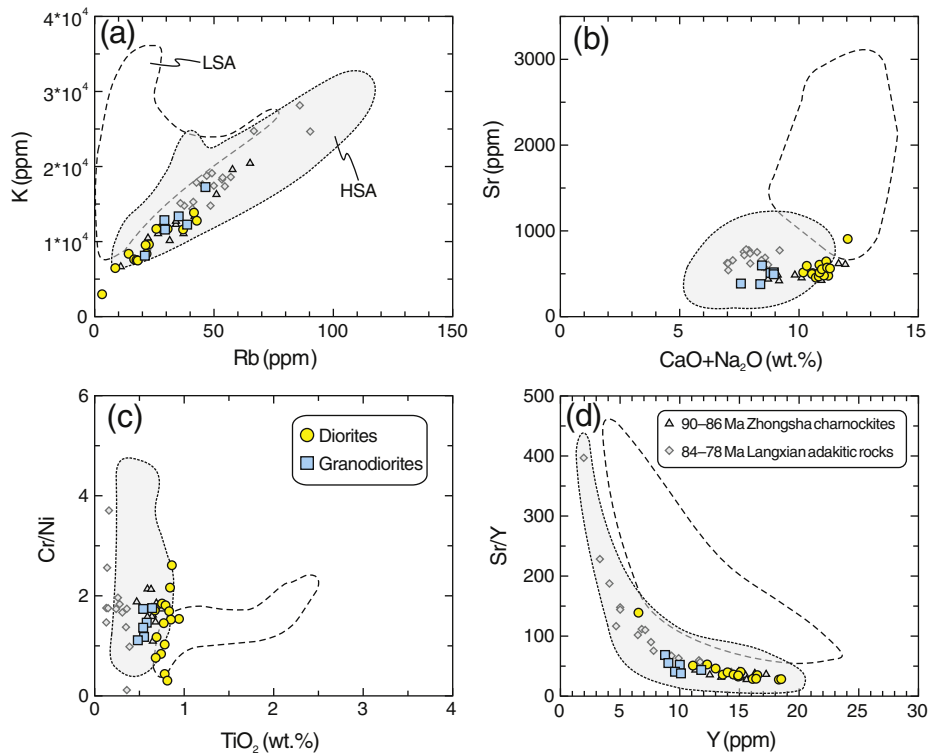
Fig. 11. Comparison between the geochemical characteristics of the Milin adakitic charnockites and the key geochemical parameters used by Martin et al. (2005) to highlight the differences between high-SiO₂ (HSA) and low-SiO₂ (LSA) adakites. (a) K ppm versus Rb ppm; (b) Sr versus CaO + Na₂O; (c) Cr/Ni versus TiO₂; (d) Sr/Y versus Y. Data sources and symbols are the same as in Fig. 4.

subducted Tethyan oceanic slab (Ma et al., 2013-a). The descending slab, migrating backwards in the asthenospheric mantle (i.e., roll-back), left low-pressure regions resulting in the upwelling of asthenosphere (Gvirtzman and Nur, 1999). This is consistent with the ~93 Ma Milin norites that contain a high-temperature and depleted asthenospheric component (flat REE patterns and high εHf(t) values) (Ma et al., 2013-a). Yogodzinski et al. (2001) suggested that adakites can be formed whenever the edge of a subducting plate is warmed up or ablated by mantle flow. Asthenospheric upwelling or the triggered mantle flow probably provided the high thermal regime (800–1000 °C at depths of 70–80 km, Sen and Dunn, 1994) required for partial melting the subducting oceanic crust to generate the Milin adakitic charnockites (Fig. 13).

We used the two-pyroxene geothermometer (Taylor, 1998) to estimate the formation temperature of the Milin adakitic charnockites. Our temperature calculations suggest that the Milin charnockitic diorites and granodiorites have high crystallization temperatures of 876 to 949 °C and 889 to 914 °C, respectively. Collectively, the coeval occurrence of high-temperature noritic and charnockitic magmatism (Ma et al., 2013-a; Zhang et al., 2010b and this study) and granulite-facies metamorphism (Zhang et al., 2010a) in the Milin area provide strong evidence for an early Late Cretaceous regional thermal event, consistent with the asthenospheric upwelling as a result of the roll-back of subducted Tethyan oceanic slab (Ma et al., 2013-a).

5.3.2. Implications for continental crustal growth

Tonalite–trondhjemite–granodiorite (TTG) comprise a large proportion of Archean felsic crust (Martin, 1999, Martin et al., 2005; Mints et al., 2010) and many compositional features of the TTGs are shared by Cenozoic adakites, which are commonly inferred to have formed by partial melting of a subducted young and hot oceanic slab. The Cenozoic rocks have been viewed as partial analogs of the Archean TTG series, although their contribution to post-Archean crustal growth is generally

considered to have been minor (Defant and Drummond, 1990; Drummond and Defant, 1990; Drummond et al., 1996; Martin, 1999; Martin and Moyen, 2002; Martin et al., 2005). In recent years, however, the contribution of recycled oceanic crust to Phanerozoic crustal growth has been demonstrated by a number of studies (e.g., Collins et al., 2011; Drummond et al., 1996; Martin et al., 2005; Tang et al., 2012). Several dynamic models have been proposed to provide the thermal requirements needed for slab melting, such as subduction of young and hot slab (e.g., Defant and Drummond, 1990), ridge subduction–slab window processes (e.g., Sisson et al., 2003; Tang et al., 2012) and low-angle or
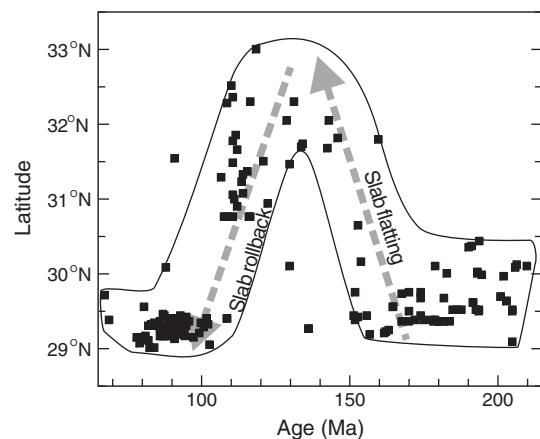

Fig. 12. U–Pb ages of magmatic rocks in the Lhasa block plotted against their latitude. The age and location data for the magmatic rocks in the Lhasa block are from these reference sources (Chu et al., 2006; Geng et al., 2006; Guan et al., 2010, 2011; Guo, 2011; Guo et al., 2011; Ji et al., 2009a,b; Jiang et al., 2012; Kang et al., 2010; Liu et al., 2006; Ma et al., 2013-a,b; Qu et al., 2007; Quidelleur et al., 1997; Scharer et al., 1984; Wen et al., 2008a,b; Xu, 2010; Zhang et al., 2010a; Zhu et al., 2011, this study and unpublished data).
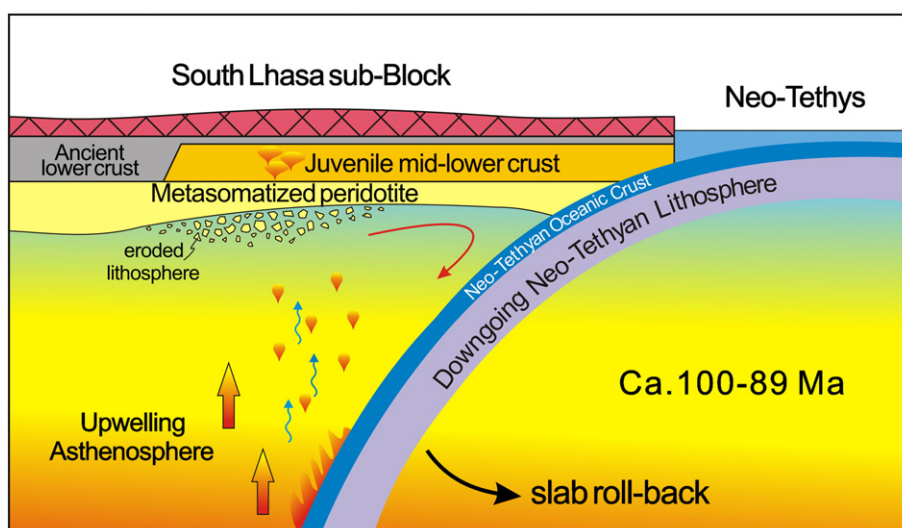
Fig. 13. The conceptual diagram illustrating the tectonic and magmatic rock evolution of the Gangdese during the early Late Cretaceous (~100–89 Ma). The upwelling asthenosphere, triggered by roll-back of subducted Neo-Tethyan oceanic lithosphere, provides the required high thermal regime for slab melting.

flat-slab subduction (e.g., Gutscher et al., 2000). Based on the results of this study, we suggest that the asthenospheric upwelling as a result of the roll-back of subducted Tethyan oceanic slab can also provide the required high thermal regime for partial melting of subducting oceanic crust (Fig. 13).

Both the Mesozoic–Early Tertiary Gangdese and the Ladakh batholiths along the southern margin of the Lhasa block consist mainly of granites with high and positive $\varepsilon_{Nd}(t)$ (up to +5.5) and $\varepsilon_{Hf}(t)$ (up to +16.5) values (e.g., Chu et al., 2011; Chung et al., 2005; Debon et al., 1986; Harris et al., 1988a,b, 1990; Ji et al., 2009a; Mo et al., 2007; Ravikant et al., 2009; Wen et al., 2008b; Zhu et al., 2011, 2012, and references therein). Previous studies suggested that they were generated by remelting of underplated juvenile basaltic crust (e.g., Chu et al., 2011; Chung et al., 2003, 2009; Ji et al., 2009a; Mo et al., 2005, 2007; Wen et al., 2008a). Mo et al. (2008) first suggested the contribution of syncollisional "slab melts" to continental crustal growth in southern Tibet. The pre-collisional (ca. 90 Ma) adakite belt, thought to have been derived from melting of subducted oceanic slab, stretches a >200 km length in the eastern Gangdese batholith along the IYTS (Fig. 1c) (e.g., Guan et al., 2010; Kang et al., 2010; Zhang et al., 2010a,b; Jiang et al., 2012 and this study). The similarities in the isotopic compositions of these slab-derived adakites to those of granitoids in the Gangdese and Ladakh batholiths (Fig. 6b) thus suggest that, in addition to mantle-derived components (Chu et al., 2006; Ji et al., 2009a,b; Ma et al., 2013-a,b; Wen et al., 2008a,b; Zhu et al., 2011), recycled oceanic crustal components also played significant role in the evolution and growth of the continental crust in the southern Lhasa block in the Mesozoic (Fig. 13).

6. Conclusions

The Milin adakitic charnockites were emplaced in the early Late Cretaceous (99–89 Ma), simultaneous with the early Late Cretaceous (ca. 100–80 Ma) magmatic "flare-up" in the southern Gangdese area. They were most probably produced by partial melting of subducted oceanic crust, followed by subsequent adakitic melt–mantle interactions, minor crustal assimilation, and fractional crystallization of amphibole + plagioclase. The upwelling asthenosphere, which was triggered by the roll-back of flatly subducted slab, provided the required heat for slab melting. In addition to pre-collisional and syn-collisional underplating of mantle-derived magmas, the results of this study demonstrate that recycling of subducted oceanic crust also played a significant role in continental crustal growth in southern Tibet.

Appendix A. Supplementary data

Supplementary data to this article can be found online at http://dx.doi.org/10.1016/j.lithos.2013.04.006.

References

Aitchison, J.C., Badengzhu, Davis, A.M., Liu, J.B., Luo, H., Malpas, J.G., McDermid, I.R.C., Wu, H.Y., Ziabrev, S.V., Zhou, M.F., 2000. Remnants of a Cretaceous intra-oceanic subduction system within the Yarlung^Zangbo suture (southern Tibet). Earth and Planetary Science Letters 183, 231–244.
Aitchison, J.C., Ali, J.R., Davis, A.M., 2007. When and where did India and Asia collide? Journal of Geophysicsal Research 112, B05423.
Aitchison, J.C., Ali, J.R., Davis, A.M., 2008. Reply to comment by Eduardo Garzanti on "When and where did India and Asia collide?". Journal of Geophysicsal Research 113, B04412.
Arculus, R.J., 2003. Use and abuse of the terms calcalkaline and calcalkalic. Journal of Petrology 44 (5), 929–935.
Armstrong, R.L., 1991. The persistent myth of crustal growth. Australian Journal of Earth Sciences 38, 613–630.
Atherton, M.P., Petford, N., 1993. Generation of sodium-rich magmas from newly underplated basaltic crust. Nature 362, 144–146.
Black, L.P., Kamo, S.L., Allen, C.M., Aleinikoff, J.N., Davis, D.W., Korsch, R.J., Foudoulis, C., 2003. TEMORA 1: a new zircon standard for Phanerozoic U–Pb geochronology. Chemical Geology 200, 155–170.
Castillo, P.R., 2006. An overview of adakite petrogenesis. Chinese Science Bulletin 51, 3257–3268.
Castillo, P.R., 2012. Adakite petrogenesis. Lithos 134, 304–315.
Castillo, P.R., Janney, P.E., Solidum, R.U., 1999. Petrology and geochemistry of Camiguin Island, southern Philippines: insights to the source of adakites and other lavas in a complex arc setting. Contributions to Mineralogy and Petrology 134, 33–51.
Chauvel, C., Blichert-Toft, J., 2001. A hafnium isotope and trace element perspective on melting of the depleted mantle. Earth and Planetary Science Letters 190, 137–151.

Chauvel, C., Lewin, E., Carpentier, M., Arndt, N.T., Marini, J.C., 2008. Role of recycled oceanic basalt and sediment in generating the Hf–Nd mantle array. Nature Geoscience 1, 64–67.

Chen, J.L., Xu, J.F., Ren, J.B., Wang, B.D., Yu, H.X., 2011. Geochemical differences between the subduction- and collisional type ore-bearing porphyric rocks. Acta Petrologica Sinica 27 (9), 2733–2742 (In Chinese with English abstract).

Chu, M.F., Chung, S.L., Song, B., Liu, D., O'Reilly, S.Y., Pearson, N.J., Ji, J., Wen, D.J., 2006. Zircon U–Pb and Hf isotope constraints on the Mesozoic tectonics and crustal evolution of southern Tibet. Geology 34, 745–748.

Chu, M.F., Chung, S.L., O'Reilly, S.Y., Pearson, N.J., Wu, F.Y., Li, X.H., Liu, D., Ji, J., Chu, C.H., Lee, H.Y., 2011. India's hidden inputs to Tibetan orogeny revealed by Hf isotopes of Transhimalayan zircons and host rocks. Earth and Planetary Science Letters 307, 479–486.

Chung, S.L., Liu, D., Ji, J., Chu, M.F., Lee, H.Y., Wen, D.J., Lo, C.H., Lee, T.Y., Qian, Q., Zhang, Q., 2003. Adakites from continental collision zones: melting of thickened lower crust beneath southern Tibet. Geology 31, 1021–1024.

Chung, S.L., Chu, M.F., Zhang, Y., Xie, Y., Lo, C.H., Lee, T.Y., Lan, C.Y., Li, X., Zhang, Q., Wang, Y., 2005. Tibetan tectonic evolution inferred from spatial and temporal variations in post-collisional magmatism. Earth-Science Reviews 68, 173–196.

Chung, S.L., Chu, M.F., Ji, J., O'Reilly, S.Y., Pearson, N., Liu, D., Lee, T.Y., Lo, C.H., 2009. The nature and timing of crustal thickening in Southern Tibet: geochemical and zircon Hf isotopic constraints from postcollisional adakites. Tectonophysics 477, 36–48.

Clift, P.D., Vannucchi, P., 2004. Controls on tectonic accretion versus erosion in subduction zones: implications for the origin and recycling of the continental crust. Reviews of Geophysics 42, RG2001. http://dx.doi.org/10.1029/2003RG000127.

Clift, P.D., Vannucchi, P., Morgan, J.P., 2009. Crustal redistribution, crust-mantle recycling and Phanerozoic evolution of the continental crust. Earth-Science Reviews 97, 80–104.

Collins, W.J., Belousova, E.A., Kemp, A.I.S., Murphy, J.B., 2011. Two contrasting Phanerozoic orogenic systems revealed by hafnium isotope data. Nature Geoscience 4, 333–337.

Coulon, C., Maluski, H., Bollinger, C., Wang, S., 1986. Mesozoic and Cenozoic volcanic rocks from central and southern Tibet: 39Ar–40Ar dating, petrological characteristics and geodynamical significance. Earth and Planetary Science Letters 79, 281–302.

Danyushevsky, L.V., Falloon, T.J., Crawford, A.J., Tetroeva, S.A., Leslie, R.L., Verbeeten, A., 2008. High-Mg adakites from Kadavu Island Group, Fiji, southwest Pacific: Evidence for the mantle origin of adakite parental melts. Geology 36 (6), 499–502.

Davidson, J., MacPherson, C., Turner, S., 2007. Amphibole control on the differentiation of arc magmas. Geochimica et Cosmochimica Acta 71, A204-A204.

Debon, F., Fort, P.L.E., Sheppard, S.M.F., Sonet, J., 1986. The four plutonic belts of the Transhimalaya–Himalaya: a chemical, mineralogical, isotopic, and chronological synthesis along a Tibet–Nepal section. Journal of Petrology 27, 219–250.

DeCelles, P.G., Kapp, P., Ding, L., Gehrels, G.E., 2007. Late Cretaceous to middle Tertiary basin evolution in the central Tibetan Plateau: changing environments in response to tectonic partitioning, aridification, and regional elevation gain. Geological Society of America Bulletin 119, 654–680.

Defant, M.J., Drummond, M.S., 1990. Derivation of some modern arc magmas by melting of young subducted lithosphere. Nature 347, 662–665.

Defant, M.J., Richerson, P.M., De Boer, J.Z., Stewart, R.H., Maury, R.C., Bellon, H., Drummond, M.S., Feigenson, M.D., Jackson, T.E., 1991. Dacite genesis via both slab melting and differentiation: petrogenesis of La Yeguada volcanic complex, Panama. Journal of Petrology 32, 1101–1142.

Defant, M.J., Drummond, M.S., 1993. Mount St. Helens: potential example of the partial melting of the subducted lithosphere in a volcanic arc. Geology 21 (6), 547–550.

DePaolo, D.J., 1988. Neodymium isotope geochemistry: an introduction. Springer-Verlag, Berlin.

Dewey, J.F., Shackleton, R.M., Chengfa, C., Yiyin, S., 1988. The tectonic evolution of the Tibetan Plateau. Philosophical transactions of the Royal Society of London. Series A. Mathematical and Physical Sciences 327, 379–413.

Drummond, M.S., Defant, M.J., 1990. A model for trondhjemite–tonalite–dacite genesis and crustal growth via slab melting: Archean to modern comparisons. Journal of Geophysical Research 95, 21503–21521.

Drummond, M.S., Defant, M.J., Kepezhinskas, P.K., 1996. Petrogenesis of slab-derived trondhjemite–tonalite–dacite/adakite magmas. Transactions of the Royal Society of Edinburgh: Earth Sciences 87, 205–215.

Feio, G.R.L., Dall'Agnol, R., Dantas, E.L., Macambira, M.J.B., Gomes, A.C.B., Sardinha, A.S., Oliveira, D.C., Santos, R.D., Santos, P.A., 2013. Geochemistry, geochronology, and origin of the Neoarchean Planalto Granite suite, Carajás, Amazonian craton: a-type or hydrated charnockitic granites? Lithos 151, 57–73.

Frost, B.R., Frost, C.D., 2008. On charnockites. Gondwana Research 13, 30–44.

Frost, B.R., Frost, C.D., Hulsebosch, T.P., Swapp, S.M., 2000. Origin of the charnockites of the Louis Lake batholith, Wind River Range, Wyoming. Journal of Petrology 41, 1759–1776.

Fyfe, W.S., 1978. The evolution of the earth's crust: modern plate tectonics to ancient hot spot tectonics? Chemical Geology 23, 89–114.

Garzanti, E., 2008. Comment on "When and where did India and Asia collide?" by Jonathan C. Aitchison, Jason R. Ali, and Aileen M. Davis. Journal of Geophysical Research 113, B04411.

Geng, Q.R., Pan, G.T., Wang, L.Q., Zhu, D.C., Liao, Z.L., 2006. Isotopic geochronology of the volcanic rocks from the Yeba Formation in the Gangdise zone, Xizang. Sedimentary Geology and Tethyan Geology 26, 1–7 (in Chinese with English abstract).

Grantham, G.H., Mendonidis, P., Thomas, R.J., Satish-Kumar, M., 2012. Multiple origins of charnockite in the Mesoproterozoic Natal belt, Kwazulu-Natal, South Africa. Geoscience Frontiers. http://dx.doi.org/10.1016/j.gsf.2012.05.006.

Guan, Q., Zhu, D.C., Zhao, Z.D., Zhang, L.L., Liu, M., Li, X.W., Yu, F., Mo, X.X., 2010. Late Cretaceous adakites in the eastern segment of the Gangdese Belt, southern Tibet: products of Neo-Tethyan ridge subduction? Acta Petrologica Sinica 26, 2165–2179.

Guan, Q., Zhu, D.C., Zhao, Z.D., Dong, G.C., Mo, X.X., Liu, Y.S., Hu, Z.C., Yuan, H.L., 2011. Zircon U–Pb chronology, geochemistry of the Late Cretaceous mafic magmatism in the southern Lhasa Terrane and its implications. Acta Petrologica Sinica 27, 2083–2094.

Guan, Q., Zhu, D.-C., Zhao, Z.-D., Dong, G.-C., Zhang, L.-L., Li, X.-W., Liu, M., Mo, X.-X., Liu, Y.-S., Yuan, H.-L., 2012. Crustal thickening prior to 38 Ma in southern Tibet: Evidence from lower crust-derived adakitic magmatism in the Gangdese Batholith. Gondwana Research 21, 88–99.

Guivel, C., Lagabrielle, Y., Bourgois, J., Martin, H., Arnaud, N., Fourcade, S., Cotten, J., Maury, R.C., 2003. Very shallow melting of oceanic crust during spreading ridge subduction: origin of near-trench Quaternary volcanism at the Chile Triple Junction. Journal of Geophysical Research 108, 2345. http://dx.doi.org/10.1029/2002JB002119.

Guo, L.S., 2011. Geochemistry and Geochronology of Mesozoic Magmatic Rocks in the Gangdes Belt, Southern Tibet: Implications for Petrogenesis and Geodynamic Setting, Geochemistry. Peking University, Beijing (140 pp.).

Guo, L., Zhang, H.-F., Harris, N., Pan, F.-B., Xu, W.-C., 2011. Origin and evolution of multi-stage felsic melts in eastern Gangdese belt: Constraints from U–Pb zircon dating and Hf isotopic composition. Lithos 127, 54–67.

Guo, Z., Wilson, M., Liu, J., 2007. Post-collisional adakites in south Tibet: products of partial melting of subduction-modified lower crust. Lithos 96, 205–224.

Gutscher, M.A., Maury, R., Eissen, J.P., Bourdon, E., 2000. Can slab melting be caused by flat subduction? Geology 28, 535–538.

Gvirtzman, Z., Nur, A., 1999. The formation of Mount Etna as the consequence of slab rollback. Nature 401, 782–785.

Harris, N., Ronghua, X., Lewis, C., Chengwei, J., 1988. Plutonic rocks of the 1985 Tibet geotraverse, Lhasa to Golmud. Philosophical Transactions of the Royal Society of London. Series A. Mathematical and Physical Sciences 327, 145–168.

Harris, N., Ronghua, X., Lewis, C., Hawkesworth, C., Yuquan, Z., 1988. Isotope geochemistry of the 1985 Tibet geotraverse, Lhasa to Golmud. Philosophical Transactions of the Royal Society of London. Series A. Mathematical and Physical Sciences 327, 263–285.

Harris, N., Inger, S., Ronghua, X., 1990. Cretaceous plutonism in Central Tibet: an example of post-collision magmatism? Journal of Volcanology and Geothermal Research 44, 21–32.

Hawkesworth, C.J., Kemp, A.I.S., 2006. Evolution of the continental crust. Nature 443, 811–817.

Hoskin, P., Black, L., 2000. Metamorphic zircon formation by solid state recrystallization of protolith igneous zircon. Journal of Metamorphic Geology 18, 423–439.

Hou, Z.-Q., Gao, Y.-F., Qu, X.-M., Rui, Z.-Y., Mo, X.-X., 2004. Origin of adakitic intrusives generated during mid-Miocene east–west extension in southern Tibet. Earth and Planetary Science Letters 220, 139–155.

Huang, X.L., Xu, Y.G., Lo, C.H., Wang, R.C., Lin, C.Y., 2007. Exsolution lamellae in a clinopyroxene megacryst aggregate from Cenozoic basalt, Leizhou Peninsula, South China: petrography and chemical evolution. Contributions to Mineralogy and Petrology 154, 691–705.

Ingle, S., Weis, D., Doucet, S., Mattielli, N., 2003. Hf isotope constraints on mantle sources and shallow-level contaminants during Kerguelen hot spot activity since 120 Ma. Geochemistry, Geophysics, Geosystems 4 (8), 1068. http://dx.doi.org/10.1029/2002GC000482.

Jahn, B.M., Wu, F.Y., Chen, B., 2000. Massive granitoid generation in Central Asia: Nd isotope evidence and implication for continental growth in the Phanerozoic. Episodes 23, 82–92.

Janardhan, A.S., Newton, R.C., Hansen, E.C., 1982. The transformation of amphibolite facies gneiss to charnockite in Southern Karnataka and northern Tamil Nadu, India. Contributions to Mineralogy and Petrology 79, 130–149.

Ji, W.Q., Wu, F.Y., Chung, S.L., Li, J.X., Liu, C.Z., 2009. Zircon U–Pb geochronology and Hf isotopic constraints on petrogenesis of the Gangdese batholith, southern Tibet. Chemical Geology 262, 229–245.

Ji, W.Q., Wu, F.Y., Liu, C.Z., Chung, S.L., 2009. Geochronology and petrogenesis of granitic rocks in Gangdese batholith, southern Tibet. Science China D 39, 849–871.

Ji, W.-Q., Wu, F.-Y., Liu, C.-Z., Chung, S.-L., 2012. Early Eocene crustal thickening in southern Tibet: New age and geochemical constraints from the Gangdese batholith. Journal of Asian Earth Sciences 53, 82–95.

Jiang, Z.Q., Wang, Q., Li, Z.X., Wyman, D.A., Tang, G.J., Jia, X.H., Yang, Y.H., 2012. Late Cretaceous (ca. 90 Ma) adakitic intrusive rocks in the Kelu area, Gangdese belt (southern Tibet): slab melting and implications for Cu–Au mineralization. Journal of Asian Earth Sciences 53, 67–81.

Kang, Z.Q., Xu, J.F., Chen, J.L., Wang, B.D., Dong, Y.H., 2010. The geochronology of Sangri Group volcanic rocks in Tibet Constraints from later Mamen intrusions. Geochimica 39, 520–530 (in Chinese with English abstract).

Kapp, P., Yin, A., Harrison, T.M., Ding, L., 2005. Cretaceous–Tertiary shortening, basin development, and volcanism in central Tibet. Geological Society of America Bulletin 117, 865–878.

Kay, R.W., Kay, S.M., 1993. Delamination and delamination magmatism. Tectonophysics 219, 177–189.

Kay, S.M., Ramos, V.A., Marquez, M., 1993. Evidence in Cerro Pampa volcanic rocks of slab melting prior to ridge trench collision in southern South America. Journal of Geology 101, 703–714.

Le Maitre, R.W., 2002. Igneous Rocks: a Classification and Glossary of Terms. Cambridge University Press, New York (236 pp.).

Li, X.H., Zhou, H., Chung, S.L., Lo, C.H., Wei, G., Liu, Y., Lee, C.Y., 2002. Geochemical and Sr–Nd isotopic characteristics of late Paleogene ultrapotassic magmatism in southeastern Tibet. International Geology Review 44, 559–574.

Li, X.H., Liu, D., Sun, M., Li, W.X., Liang, X.R., Liu, Y., 2004. Precise Sm–Nd and U–Pb isotopic dating of the supergiant Shizhuyuan polymetallic deposit and its host granite, SE China. Geological Magazine 141, 225.

Li, X.H., Qi, C.S., Liu, Y., Liang, X.R., Tu, X.L., Xie, L.W., Yang, Y.H., 2005. Petrogenesis of the Neoproterozoic bimodal volcanic rocks along the western margin of the Yangtze

Block: new constraints from Hf isotopes and Fe/Mn ratios. Chinese Science Bulletin 50, 2481–2486.

Li, J.W., Zhao, X.F., Zhou, M.F., Ma, C.Q., de Souza, Z., Vasconcelos, P., 2009. Late Mesozoic magmatism from the Daye region, eastern China: U–Pb ages, petrogenesis, and geodynamic implications. Contributions to Mineralogy and Petrology 157, 383–409.

Liu, Q.S., Jiang, W., Jian, P., Wu, Z.H., Hu, D.G., 2006. Zircon SHRIMP age and petrochemical and geochemical features of Mesozoic muscovite monzonitic granilite at Ningzhong, Tibet. Acta Petrologica Sinca 22 (3), 643–652 (In Chinese with English abstract).

Ma, L., Wang, Q., Li, Z.X., Wyman, D.A., Jiang, Z.Q., Yang, J.H., Gou, G.N., Guo, H.F., 2013. The early Late Cretaceous (ca. 93 Ma) norites and hornblendites in the Milin area, eastern Gangdese: lithosphere–asthenosphere interaction during slab roll-back and an insight into early Late Cretaceous (ca. 100–80 Ma) magmatic "flare-up" in southern Lhasa (Tibet). Lithos 172–173, 17–30.

Ma, L., Wang, Q., Wyman, D.A., Jiang, Z.Q., Yang, J.H., Li, Q.L., Gou, G.N., Guo, H.F., 2013. Late Cretaceous crustal growth in the Gangdese area, southern Tibet: petrological and Sr–Nd–Hf–O isotopic evidence from Zhengga diorite–gabbro. Chemical Geology. http://dx.doi.org/10.1016/j.chemgeo.2013.04.005 (in press-b).

Macpherson, C.G., Dreher, S.T., Thirlwall, M.F., 2006. Adakites without slab melting: high pressure differentiation of island arc magma, Mindanao, the Philippines. Earth and Planetary Science Letters 243, 581–593.

Mahoney, J.J., Frei, R., Tejada, M., Mo, X., Leat, P., Nägler, T., 1998. Tracing the Indian Ocean mantle domain through time: isotopic results from old West Indian, East Tethyan, and South Pacific seafloor. Journal of Petrology 39, 1285–1306.

Malpas, J., Zhou, M.F., Robinson, P.T., Reynolds, P.H., 2003. Geochemical and geochronological constraints on the origin and emplacement of the Yarlung Zangbo ophiolites, Southern Tibet. Geological Society, London, Special Publications 218, 191–206.

Martin, H., 1999. Adakitic magmas: modern analogues of Archean granitoids. Lithos 46, 411–429.

Martin, H., Moyen, J.F., 2002. Secular changes in tonalite–trondhjemite–granodiorite composition as markers of the progressive cooling of Earth. Geology 30, 319–322.

Martin, H., Smithies, R., Rapp, R., Moyen, J.F., Champion, D., 2005. An overview of adakite, tonalite–trondhjemite–granodiorite (TTG), and sanukitoid: relationships and some implications for crustal evolution. Lithos 79, 1–24.

Middlemost, E.A.K., 1994. Naming materials in the magma/igneous rock system. Earth-Science Reviews 37, 215–224.

Mints, M.V., Belousova, E.A., Konilov, A.N., Natapov, L.M., Shchipansky, A.A., Griffin, W.L., O'Reilly, S.Y., Dokukina, K.A., Kaulina, T.V., 2010. Mesoarchean subduction processes: 2.87 Ga eclogites from the Kola Peninsula, Russia. Geology 38, 739–742.

Miyashiro, A., 1974. Volcanic rock series in island arcs and active continental margins. American Journal of Science 274 (4), 321.

Mo, X.X., Dong, G.C., Zhao, Z.D., Guo, T.Y., Wang, L.L., Chen, T., 2005. Timing of magma mixing in the Gangdisê Magmatic Belt during the India–Asia collision: zircon SHRIMP U–Pb dating. Acta Geologica Sinica-English Edition 79, 66–76.

Mo, X.X., Zhao, Z.D., Deng, J.F., Martin, H., Yu, X.H., Luo, Z.H., Li, Y.G., Zhou, S., Dong, G.C., Zhu, D.C., Wang, L.L., 2006. Petrology and geochemistry of postcollisional volcanic rocks from the Tibetan plateau: implications for lithosphere heterogeneity and collision-induced asthenospheric mantle flow. Geological Society of America Special Papers 409, 507–530.

Mo, X., Hou, Z., Niu, Y., Dong, G., Qu, X., Zhao, Z., Yang, Z., 2007. Mantle contributions to crustal thickening during continental collision: evidence from Cenozoic igneous rocks in southern Tibet. Lithos 96, 225–242.

Mo, X., Niu, Y., Dong, G., Zhao, Z., Hou, Z., Zhou, S., Ke, S., 2008. Contribution of syncollisional felsic magmatism to continental crust growth: a case study of the Paleogene Linzizong volcanic succession in southern Tibet. Chemical Geology 250, 49–67.

Moyen, J.F., 2009. High Sr/Y and La/Yb ratios: the meaning of the "adakitic signature". Lithos 112, 556–574.

Moyen, J.F., Stevens, G., Kisters, A.F.M., Belcher, R.W., 2007. TTG plutons of the Barberton granitoid-greenstone terrain, South Africa. In: Van Kranendonk, M.J., Smithies, R.H., Bennet, V. (Eds.), Earth's Oldest rocks. Developments in Precambrian geology. Elsevier, pp. 606–668.

Murphy, M.A., Yin, A., Harrison, T.M., Dürr, S.B., Chen, Z., Ryerson, F.J., Kidd, W.S.F., Wang, X., Zhou, X., 1997. Did the Indo–Asian collision alone create the Tibetan Plateau? Geology 25, 719–722.

Niu, Y., Batiza, R., 1997. Trace element evidence from seamounts for recycled oceanic crust in the eastern equatorial Pacific mantle. Earth and Planetary Science Letters 148, 471–484.

Pan, G.T., Mo, X.X., Hou, Z.Q., Zhu, D.C., Wang, L.Q., Li, G.M., Zhao, Z.D., Geng, Q.R., Liao, Z.L., 2006. Spatial-temporal framework of the Gangdese Orogenic Belt and its evolution. Acta Petrologica Sinica 22 (3), 521–533 (in Chinese with English abstract).

Peacock, S.M., Rushmer, T., Thompson, A.B., 1994. Partial melting of subducting oceanic-crust. Earth and Planetary Science Letters 121, 227–244.

Peccerillo, A., Taylor, S.R., 1976. Geochemistry of Eocene calc-alkaline volcanic rocks from the Kastamonu area, Northern Turkey. Contributions to Mineralogy and Petrology 58 (1), 63–81.

Plank, T., 2005. Constraints from thorium/lanthanum on sediment recycling at subduction zones and the evolution of the continents. Journal of Petrology 46 (5), 921–944.

Plank, T., Langmuir, C.H., 1998. The chemical composition of subducting sediment and its consequences for the crust and mantle. Chemical Geology 145, 325–394.

Qu, X.M., Xin, H.B., Xu, W.Y., 2007. Petrogenesis of the Ore-Hosting Volcanic Rocks and Their Contribution to Mineral ization in Xiongcun Superlarge Cu-Au Deposit, Tibet. Acta Geologica Sinica 81, 964–971 (in Chinese with English abstract).

Quidelleur, X., Grove, M., Lovera, O.M., Harrison, T.M., Yin, A., Ryerson, F., 1997. Thermal evolution and slip history of the Renbu Zedong Thrust, southeastern Tibet. Journal of Geophysical Research, All Series 102, 2659–2679.

Rapp, R.P., Watson, E.B., 1995. Dehydration melting of metabasalt at 8–32 kbar: implications for continental growth and crust-mantle recycling. Journal of Petrology 36, 891–931.

Rapp, R.P., Shimizu, N., Norman, M.D., Applegate, G.S., 1999. Reaction between slab derived melts and peridotite in the mantle wedge: experimental constraints at 3.8 GPa. Chemical Geology 160, 335–356.

Ravikant, V., Wu, F.Y., Ji, W.Q., 2009. Zircon U–Pb and Hf isotopic constraints on petrogenesis of the Cretaceous–Tertiary granites in eastern Karakoram and Ladakh, India. Lithos 110, 153–166.

Rudnick, R.L., 1995. Making continental crust. Nature 378, 571–578.

Rudnick, R.L., Gao, S., 2003. The composition of the continental crust. In: Rudnick, R.L. (Ed.), The Crust. Elsevier–Pergamon, Oxford, pp. 1–64.

Schaltegger, U., Zeilinger, G., Frank, M., Burg, J.P., 2002. Multiple mantle sources during island arc magmatism. U–Pb and Hf isotopic evidence from the Kohistan Arc Complex, Pakistan. Terra Nova 14, 461–468.

Scharer, U., Xu, R.H., Allegre, C.J., 1984. U–Pb geochronology of Gangdese (Transhimalaya) plutonism in the Lhasa–Xigaze region, Tibet. Earth and Planetary Science Letters 69, 311–320.

Sen, C., Dunn, T., 1994. Dehydration melting of a basaltic composition amphibolite at 1.5 and 2.0 GPa: implications for the origin of adakites. Contributions to Mineralogy and Petrology 117, 394–409.

Shimoda, G., Tatsumi, Y., Nohda, S., Ishizaka, K., Jahn, B.M., 1998. Setouchi high-Mg andesites revisited: geochemical evidence for melting of subducting sediments. Earth and Planetary Science Letters 160 (3–4), 479–492.

Sisson, V.B., Poole, A.R., Harris, N.R., Burner, H.C., Pavlis, T.L., Copeland, P., Donelick, R.A., McLelland, W.C., 2003. Geochemical and geochronologic constraints for genesis of a tonalite–trondhjemite suite and associated mafic intrusive rocks in the eastern Chugach Mountains, Alaska: a record of ridge-transform subduction. Special Papers-Geological Society of America 293–326.

Smithies, R., 2000. The Archean tonalite–trondhjemite–granodiorite (TTG) series is not an analogue of Cenozoic adakite. Earth and Planetary Science Letters 182, 115–125.

Stern, C.R., Kilian, R., 1996. Role of the subducted slab, mantle wedge and continental crust in the generation of adakites from the Andean Austral Volcanic Zone. Contributions to Mineralogy and Petrology 123 (3), 263–281.

Streck, M.J., Leeman, W.P., Chesley, J., 2007. High-Mg andesite from Mount Shasta: a product of magma mixing and contamination, not a primitive mantle melt. Geology 35, 351–354.

Sun, S.S., McDonough, W.F., 1989. Chemical and isotopic systematics of oceanic basalts: implications for mantle composition and processes. In: Saunders, A.D., Norry, M.J. (Eds.), Magmatism in the Ocean Basins. Geological Society London Special Publications, pp. 313–345.

Tanaka, T., Togashi, S., Kamioka, H., Amakawa, H., Kagami, H., Hamamoto, T., Yuhara, M., Orihashi, Y., Yoneda, S., Shimizu, H., Kunimaru, T., Takahashi, K., Yanagi, T., Nakano, T., Fujimaki, H., Shinjo, R., Asahara, Y., Tanimizu, M., Dragusanu, C., 2000. JNdi-1. A neodymium isotopic reference in consistency with LaJolla neodymium. Chemical Geology 168, 279–281.

Tang, G.J., Wang, Q., Wyman, D.A., Li, Z.X., Xu, Y.G., Zhao, Z.H., 2012. Recycling oceanic crust for continental crustal growth: Sr–Nd–Hf isotope evidence from granitoids in the western Junggar region, NW China. Lithos 128–131, 73–83.

Tatsumi, Y., Suzuki, T., Kawabata, H., Sato, K., Miyazaki, T., Chang, Q., Takahashi, T., Tani, K., Shibata, T., Yoshikawa, M., 2006. The petrology and geochemistry of Oto-Zan composite lava flow on Shodo-Shima Island, SW Japan: Remelting of a solidified high-mg andesite magma. Journal of Petrology 47 (3), 595–629.

Taylor, W.R., 1998. An experimental test of some geothermometer and geobarometer formulations for upper mantle peridotites with application to the thermobarometry of fertile Iherzolite and garnet websterite. Neues Jahrbuch Fur MineralogieAbhandlungen 172, 381–408.

Thorkelson, D.J., 1996. Subduction of diverging plates and the principles of slab window. Tectonophysic 255, 47–63.

Thorkelson, D.J., Breitsprecher, K., 2005. Partial melting of slab window margins: genesis of adakitic and non-adakitic magmas. Lithos 79 (1–2), 25–41.

Wang, Q., Xu, J.F., Jian, P., Bao, Z.W., Zhao, Z.H., Li, C.F., Xiong, X.L., Ma, J.L., 2006. Petrogenesis of adakitic porphyries in and extensional tectonic setting, Dexing, South China: implications for the Genesis of porphyry copper mineralization. Journal of Petrology 47, 119–144.

Wang, Q., Wyman, D.A., Zhao, Z.H., Xu, J.F., Bai, Z.H., Xiong, X.L., Dai, T.M., Li, C.F., Chu, Z.Y., 2007. Petrogenesis of Carboniferous adakites and Nb-enriched arc basalts in the Alataw area, northern Tianshan Range (western China): implications for Phanerozoic crustal growth in the Central Asia orogenic belt. Chemical Geology 236, 42–64.

Wang, Q., Wyman, D.A., Xu, J., Dong, Y., Vasconcelos, P.M., Pearson, N., Wan, Y., Dong, H., Li, C., Yu, Y., Zhu, T., Feng, X., Zhang, Q., Zi, F., Chu, Z., 2008. Eocene melting of subducting continental crust and early uplifting of central Tibet: evidence from central-western Qiangtang high-K calc-alkaline andesites, dacites and rhyolites. Earth and Planetary Science Letters 272, 158–171.

Wei, G.J., Liang, X.R., Li, X.H., Liu, Y., 2002. Precise measurement of Sr isotopic compositions of liquid and solid base using (LP) MC ICP-MS. Geochimica 31, 295–305 (in Chinese with English abstract).

Wen, D.R., 2007. The Gangdese Batholith, southern Tibet: ages, geochemical characteristics and petrogenesis. National Taiwan University, Taibei (140 pp.).

Wen, D.R., Chung, S.L., Song, B., Iizuka, Y., Yang, H.J., Ji, J., Liu, D., Gallet, S., 2008. Late Cretaceous Gangdese intrusions of adakitic geochemical characteristics, SE Tibet: petrogenesis and tectonic implications. Lithos 105, 1–11.

Wen, D.R., Liu, D., Chung, S.L., Chu, M.F., Ji, J., Zhang, Q., Song, B., Lee, T.Y., Yeh, M.W., Lo, C.H., 2008. Zircon SHRIMP U–Pb ages of the Gangdese batholith and implications for Neotethyan subduction in southern Tibet. Chemical Geology 252, 191–201.

Wu, F.Y., Jahn, B.M., Wilde, S., Sun, D.Y., 2000. Phanerozoic crustal growth: U–Pb and Sr−Nd isotopic evidence from the granites in northeastern China. Tectonophysics 328, 89–113.

Wu, F.Y., Yang, Y.H., Xie, L.W., Yang, J.H., Xu, P., 2006. Hf isotopic compositions of the standard zircons and baddeleyites used in U–Pb geochronology. Chemical Geology 234, 105–126.

Xie, L.W., Zhang, Y.B., Zhang, H.H., Sun, J.F., Wu, F.Y., 2008. In situ simultaneous determination of trace elements, U–Pb and Lu–Hf isotopes in zircon and baddeleyite. Chinese Science Bulletin 53, 1565–1573.

Xu, J.-F., Shinjo, R., Defant, M.J., Wang, Q., Rapp, R.P., 2002. Origin of Mesozoic adakitic intrusive rocks in the Ningzhen area of east China: Partial melting of delaminated lower continental crust? Geology 30, 1111–1114.

Xu, J.F., Castillo, P.R., 2004. Geochemical and Nd–Pb isotopic characteristics of the Tethyan asthenosphere: implications for the origin of the Indian Ocean mantle domain. Tectonophysics 393, 9–27.

Xu, W.C., 2010. Spatical variation of zircon U–Pb ages and Hf isotopic compositions of the Gangdese granitoids and its geologic implications, Geochemistry. China University of Geosciences, Wuhan (172 pp.).

Yin, A., Harrison, T.M., 2000. Geologic evolution of the Himalayan–Tibetan orogen. Annual Review of Earth and Planetary Sciences 28, 211–280.

Yin, G.H., Chen, Y.M., Su, X.J., Bao, J.Y., Hou, S.Y., Lv, Y., Duan, G.X., Zhang, J.Y., Liu, Z., Xiao, L., 2013. 1: 250, 000 geological report of sangri County with geological map. Yunnan Province Geology Survey (in press, in Chinese).

Yogodzinski, G.M., Kay, R.W., Volynets, O.N., Koloskov, A.V., Kay, S.M., 1995. Magnesian andesite in the western Aleutian Komandorsky region: implications for slab melting and processes in the mantle wedge. Geological Society of America Bulletin 107, 505–519.

Yogodzinski, G., Lees, J., Churikova, T., Dorendorf, F., Woerner, G., Volynets, O., 2001. Geochemical evidence for the melting of subducting oceanic lithosphere at plate edges. Nature 409, 500–504.

Zahirovic, S., Müller, R.D., Seton, M., Flament, N., Gurnis, M., Whittaker, J., 2012. Insights on the kinematics of the India–Eurasia collision from global geodynamic models. Geochemistry, Geophysics, Geosystems 13, Q04W11.

Zhang, K.J., Xia, B.D., Wang, G.M., Li, Y.T., Ye, H.F., 2004. Early Cretaceous stratigraphy, depositional environments, sandstone provenance, and tectonic setting of central Tibet, western China. Geological Society of America Bulletin 116 (9–10), 1202–1222.

Zhang, S.Q., Mahoney, J., Mo, X.X., Ghazi, A., Milani, L., Crawford, A., Guo, T.Y., Zhao, Z.D., 2005. Evidence for a widespread Tethyan upper mantle with Indian-Ocean-type isotopic characteristics. Journal of Petrology 46, 829.

Zhang, Z.M., Wang, J.L., Dong, X., Zhao, G.C., Yu, F., Wang, W., Liu, F., Geng, G.S., 2009. Petrology and geochronology of the charnockite from the southern Gangdese blet: evidence for the Andean-type orogen. Acta Geologica Sinica 25, 1707–1720 (in Chinese with English abstract).

Zhang, Z.M., Zhao, G.C., Santosh, M., Wang, J.L., Dong, X., Liou, J.G., 2010. Two stages of granulite facies metamorphism in the eastern Himalayan syntaxis, south Tibet: petrology, zircon geochronology and implications for the subduction of Neo Tethys and the Indian continent beneath Asia. Journal of Metamorphic Geology 28, 719–733.

Zhang, Z.M., Zhao, G.C., Santosh, M., Wang, J.L., Dong, X., Shen, K., 2010. Late Cretaceous charnockite with adakitic affinities from the Gangdese batholith, southeastern Tibet: evidence for Neo-Tethyan mid-ocean ridge subduction? Gondwana Research 17, 615–631.

Zhang, Z.M., Shen, K., Santosh, M., Dong, X., 2011. High density carbonic fluids in a slab window: evidence from the Gangdese charnockite, Lhasa terrane, southern Tibet. Journal of Asian Earth Sciences 42, 515–524.

Zhang, K.J., Zhang, Y.X., Tang, X.C., Xia, B., 2012. Late Mesozoic tectonic evolution and growth of the Tibetan plateau prior to the Indo–Asian collision. Earth Science Review 114, 236–249.

Zhu, D.C., Pan, G.T., Chung, S.L., Liao, Z.L., Wang, L.Q., Li, G.M., 2008. SHRIMP zircon age and geochemical constraints on the origin of Lower Jurassic volcanic rocks from the Yeba Formation, southern Gangdese, South Tibet. International Geology Review 50, 442–471.

Zhu, D.C., Mo, X.X., Niu, Y.L., Zhao, Z.D., Wang, L.Q., Liu, Y.S., Wu, F.Y., 2009. Geochemical investigation of Early Cretaceous igneous rocks along an east–west traverse throughout the central Lhasa Terrane, Tibet. Chemical Geology 268, 298–312.

Zhu, D.C., Zhao, Z.D., Pan, G.T., Lee, H.Y., Kang, Z.Q., Liao, Z.L., Wang, L.Q., Li, G.M., Dong, G.C., Liu, B., 2009. Early cretaceous subduction-related adakite-like rocks of the Gangdese Belt, southern Tibet: products of slab melting and subsequent melt-peridotite interaction? Journal of Asian Earth Sciences 34, 298–309.

Zhu, D.C., Zhao, Z.D., Niu, Y., Mo, X.X., Chung, S.L., Hou, Z.Q., Wang, L.Q., Wu, F.Y., 2011. The Lhasa Terrane: record of a microcontinent and its histories of drift and growth. Earth and Planetary Science Letters 301, 241–255.

Zhu, D.C., Zhao, Z.D., Niu, Y., Dilek, Y., Hou, Z.Q., Mo, X.X., 2012. The origin and pre-Cenozoic evolution of the Tibetan Plateau. Gondwana Research. http://dx.doi.org/10.1016/j.gr.2012.1002.1002.